U.PORTO
FACULDADE DE CIÊNCIAS
UNIVERSIDADE DO PORTO

MSc

2.º
CICLO

FCUP
INESCTEC
2021

U.PORTO

High Power Fiber Laser for Space Applications

Fernando Augusto Ortigão Festas Maia

FC

U.PORTO
FACULDADE DE CIÊNCIAS
UNIVERSIDADE DO PORTO

INESCTEC
TECHNOLOGY & SCIENCE
ASSOCIATE LABORATORY
PORTUGAL

# High Power Fiber Laser for Space Applications

Fernando Augusto Ortigão Festas Maia

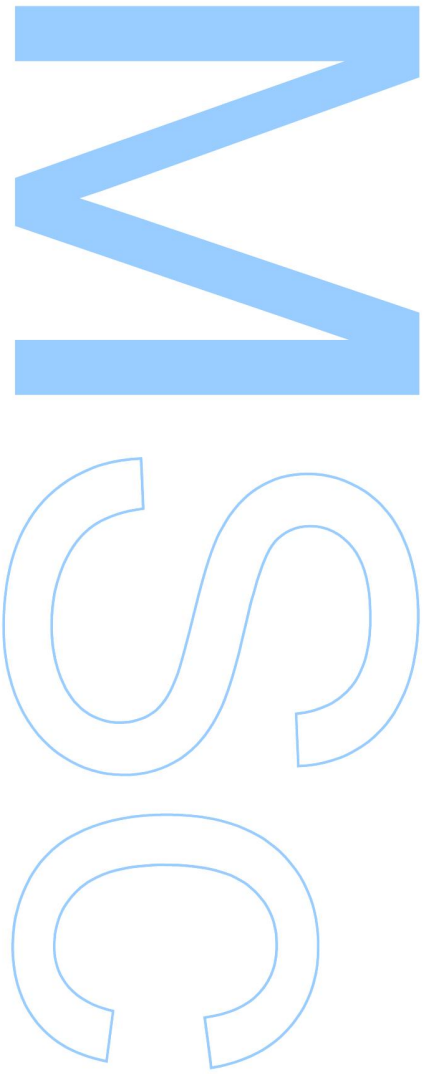
Dissertação de Mestrado em Engenharia Física apresentada à Faculdade de Ciências da Universidade do Porto

2021

# High Power Fiber Laser for Space Applications

Fernando Augusto Ortigão Festas Maia
Mestrado Integrado em Engenharia Física
Departamento de Física e Astronomia da Faculdade de Ciências da Universidade do Porto
2021

**Orientador**
Orlando Frazão, Investigador e Docente, FCUP & INESCTEC





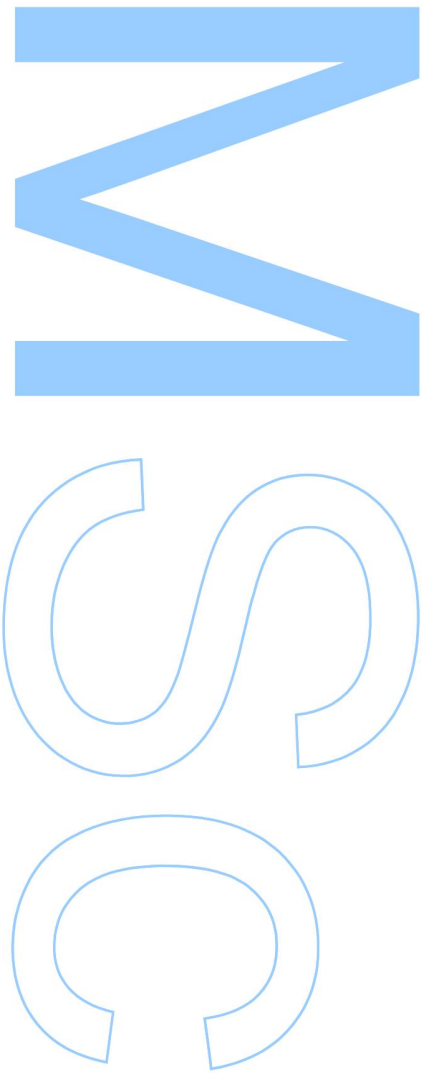




Todas as correções determinadas pelo júri, e só essas, foram efetuadas.

O Presidente do Júri,

Porto, _____/_____/_____



UNIVERSIDADE DO PORTO

MASTERS THESIS

# High Power Fiber Laser for Space Applications

*Author:*
Fernando MAIA

*Supervisor:*
Orlando FRAZÃO

*A thesis submitted in fulfilment of the requirements*
*for the degree of MSc. Engineering Physics*

*at the*

Faculdade de Ciências da Universidade do Porto
Departamento de Física e Astronomia

November 15, 2021

*" You know it has its own space*
*The horizon echoes the striking blast*
*But once the limit you cross*
*Free you'll be from present and past "*

written by Sofia Beco

# *Acknowledgements*

During the process of writing this master thesis, I received a lot of support and assistance.

First, I would like to thank my supervisor, Professor Orlando Frazão, whose expertise was invaluable in formulating the research questions and methodology. Your insightful feedback pushed me to sharpen my thinking and brought my work to a higher level.

I also would like to thank Paulo Robalinho for his dedicated work in helping me develop the laser system. Obviously, this complex system could not be installed without his countless effort. During this dissertation, I always benefited from numerous stimulating discussions with him.

I wish to thank all people that are in WiPTherm Project, for giving their best every day towards an innovative solution.

A special thank you to INESCTEC for giving me the opportunity to feel what it's like to be a researcher.

I also would like to thank Paulo Marques and João Viana Lopes who gave me the boost I needed for my simulations.

I would like to thank my parents and my sister for their endless love and constant support. You were always there for me, always put me as a priority. I am lucky to be part of this family and I hope one day I can give back to you.

Thank you Phase Transition, for being unique human beings and for giving me the opportunity of channelling musical inspiration. It is a privilege to be part of such a super musical group. Life is indeed wonderful with friends like you.

Last but definitely not least, thank you Sofia for being by my side since I started studying Engineering Physics. You were always able to put things in perspective and provide inspiration when all the things seemed too much to handle.

UNIVERSIDADE DO PORTO

# *Abstract*

Faculdade de Ciências da Universidade do Porto
Departamento de Física e Astronomia

MSc. Engineering Physics

**High Power Fiber Laser for Space Applications**

by Fernando MAIA

In the work leading to this dissertation, we built and tested a setup that allows the generation of a continuous-wave double-clad fiber laser source with its principal peak of the spectrum at 1566 $nm$ and with a maximum output power of 15 $W$. By measuring the output laser power as a function of the input pump power, we get a slope efficiency of 19%. The special fiber was created in the University of Limoges, in XLIM, by Raphaël Jamier, Baptiste Leconte et al.

We also studied a Gaussian beam profile throughout its propagation in free space. Using the angular spectrum method combined with random phase Von Karman phase screens, it was possible to simulate Gaussian beam propagation at 1550 $nm$ under turbulent conditions, and conclude that after a propagation of 7 $km$, the beam deflects on average 23.69 $mm$.

This work is supported by funding from the European Union's Horizon 2020 research and innovation program under grant agreement No 863307, Ref. H2020-FETOPEN-2018-2019-2020-01 .

UNIVERSIDADE DO PORTO

# *Resumo*

Faculdade de Ciências da Universidade do Porto
Departamento de Física e Astronomia

Mestrado Integrado em Engenharia Física

**Laser de alta potência em fibra para aplicações espaciais**

por Fernando MAIA

No trabalho conducente a esta dissertação, construímos uma fonte laser contínua em fibra de duplo revestimento com o seu pico principal a 1566 $nm$ e com uma potência máxima de saída de 15$W$, com uma arquitetura mista. Ao medir a potência de saída do laser em função da potência de entrada do laser de bombeamento, obtivemos uma eficiência de 19%. A fibra especial foi criada na Universidade de Limoges, no XLIM, por Raphaël Jamier, Baptiste Leconte e colaboradores.

É também estudado o perfil de um feixe Gaussiano ao longo da sua propagação no espaço livre. Usando o método espetral angular combinado com máscaras de fase de Von Karman aleatórias, foi possível simular a propagação do feixe Gaussiano a 1550 $nm$ em condições de turbulência, e concluir que após uma propagação de 7 $km$, o feixe deflecte em média 23.69 $mm$.

Este trabalho é apoiado pelo financiamento do programa de investigação e inovação Horizon 2020 da União Europeia ao abrigo do acordo de subvenção n.º 863307, Ref. H2020-FETOPEN-2018-2019-2020-01

# Contents

**Acknowledgements** v

**Abstract** vii

**Resumo** ix

**Contents** xi

**List of Figures** xiii

**Glossary** xv

**1 Introduction** 1
- 1.1 Context and Motivation . . . 1
- 1.2 Objectives . . . 3
- 1.3 Document Structure . . . 3
- 1.4 Outputs . . . 3

**2 Lasers' Fundamentals** 5
- 2.1 Introduction . . . 5
- 2.2 Laser Technology . . . 7
  - 2.2.1 Working principles . . . 7
  - 2.2.2 Groundbreaking work using lasers . . . 10
  - 2.2.3 Fiber lasers - an introduction . . . 12

**3 Fiber Lasers - A Brief Review** 15
- 3.1 A Brief Review . . . 15
  - 3.1.1 Atmospherical considerations . . . 17
- 3.2 Concluding Remarks . . . 19

**4 Beam Propagation Analysis** 21
- 4.1 Natural divergence of a Gaussian beam . . . 21
  - 4.1.1 Theoretical principles of divergence . . . 21
  - 4.1.2 Waist prediction . . . 22
- 4.2 Analysis of light propagation under turbulent atmospheric conditions . . . 25
  - 4.2.1 Angular Spectrum Method . . . 26
  - 4.2.2 Atmospheric Turbulence . . . 27

4.2.3 Simulation's algorithm . . . 31
4.3 Simulation results . . . 34
4.3.1 Preliminary results . . . 34
4.3.2 Results using the atmospheric layer model . . . 37
4.4 Final remarks and future work . . . 46

**5 High-Power Fiber Laser** **49**
5.1 Experimental Setup . . . 49
5.2 Results and discussion . . . 53
5.3 Final remarks . . . 56

**6 Conclusion and Future Work** **57**

**A Used AOTools functions** **59**

**Bibliography** **61**

# List of Figures


1.1 Concept of WiPTherm project [4]. . . . 2
1.2 WiPTherm project Work Packages description [4]. . . . 2

2.1 Scheme of the electromagnetic spectrum [7]. . . . 6
2.2 Schematic illustration of the three processes: (a) spontaneous emission, (b) stimulated emission, (c) absorption. . . . 8
2.3 Scheme of a 3 level laser. . . . 9
2.4 Laser cavity scheme. . . . 9
2.5 First working laser - by Theodore Maiman [14]. . . . 10
2.6 Fiber grating scheme [43]. . . . 12
2.7 Fiber grating cavity scheme [44]. . . . 13
2.8 Simple fiber laser scheme [46]. . . . 13

3.1 Schematic representation of a double-clad fiber [57]. . . . 16
3.2 Typical absorption and emission spectra of Erbium ions [74]. . . . 18

4.1 Model for 1 $m$: (a) minimization of $w_1$, (b) $w_{min}$ function of the distance. . . . 23
4.2 Model for 1 $km$: (a) minimization of $w_1$, (b) $w_{min}$ function of the distance. . . . 23
4.3 Model for 500 $km$: (a) minimization of $w_1$, (b) $w_{min}$ function of the distance. 24
4.4 Model for 1 $km$ with scaled cross-sectional dimensions, of CubeSat and laser beam. . . . 24
4.5 Visualization of waist over 1 $km$ for different values of $\omega_0$: (a) zoom of a region from main plot, (b) main plot. . . . 25
4.6 The Starry Night by Vincent van Gogh (1889 painting) [88]. . . . 27
4.7 Common models for atmospheric power spectra [99]. . . . 28
4.8 Example of a phase screen generated with a function from AOtools. . . . 31
4.9 Flow chart of the developed code. . . . 33
4.10 Turbulent atmospheric propagation simulation scheme. . . . 34
4.11 Initial Gaussian beam. . . . 35
4.12 1 $km$ free propagation of the initial Gaussian beam. . . . 35
4.13 1 $km$ propagation of the initial Gaussian beam with turbulence, $r_0 = 18.99\ m$ 36
4.14 1$km$ turbulent propagation of the initial Gaussian beam with turbulence, $r_0 = 1\ m$ . . . 37
4.15 Simulation scheme for 7000 $m$ propagation . . . 38
4.16 Beam profile after 19 $m$ of free propagation. . . . 39
4.17 Turbulent Phase Screen placed at $19^+$ $m$. . . . 39
4.18 Beam profile after 230 $m$. . . . 40
4.19 Turbulent Phase Screen placed at $230^+$ $m$. . . . 40

4.20 Beam profile after 850 $m$. . . . . 41
4.21 Turbulent Phase Screen placed at $850^{+}$ $m$. . . . . 41
4.22 Beam profile after 2000 $m$. . . . . 42
4.23 Turbulent Phase Screen placed at $2000^{+}$ $m$. . . . . 42
4.24 Beam profile after 7000 $m$. . . . . 43
4.25 Beam profile after 7000 $m$ with different random PS. . . . . 44
4.26 1000 different centers of Gaussian beams after propagating 7 $km$ of turbulent atmosphere. . . . . 45
4.27 Histogram of the center of the beam deviation after 7 $km$ of turbulent atmosphere with respective fit. . . . . 45

5.1 Sectional cut of the fiber. . . . . 50
5.2 Refractive index profile of the developed fiber analysed at 633 $nm$ with IFA-100. The right bar represents the differential values of the refractive index. . 51
5.3 Laser pump spectrum provided by the manufacturer datasheet. Vertical axis will represent optical intensity. . . . . 51
5.4 Pump power as a function of the supplied current, from the data sheet 5.4. . 52
5.5 Experimental setup of the High Power Fiber Laser . . . . . 53
5.6 Picture from the real setup. . . . . 54
5.7 Output Laser Power as a function of the pump power. . . . . 54
5.8 Spectrum of the Output Laser. . . . . 55

# Glossary

| | |
|---|---|
| **ASE** | Amplified Spontaneous Emission |
| **CAGR** | Compound Annual Growth Rate |
| **CPA** | Chirped Pulse Amplification |
| **CW** | Continuous Wave |
| **FBG** | Fiber Bragg Grating |
| **FFT** | Fast Fourier Transform |
| **FP** | Free Propagation |
| **ICF** | Inertial Confinement Fusion |
| **IFFT** | Inverse Fast Fourier Transform |
| **LASER** | light amplification by stimulated emission of radiation |
| **LMA** | Large Mode Area |
| **MASER** | Microwave Amplification by Stimulated Emission of Radiation |
| **MOPA** | Master Oscillator Power Amplifier |
| **MVKS** | Modified Von Karman Spectra |
| **NA** | Numerical Aperture |
| **OSA** | Optical Spectrum Analyzer |
| **PS** | Phase Screen |
| **PSD** | Power Spectral Density |
| **RIP** | Refractive Index Profile |
| **SWIR** | Short Wave Infra Red |
| **VKS** | Von Karman Spectrum |

**WET** Wireless Energy Transfer

**WP** Work Package

*This thesis is dedicated to my family, for their love and support.*

# Chapter 1

# Introduction

## 1.1 Context and Motivation

Over the past sixteen years, fiber lasers have been a prosperous technology due to their recent progress. The advances of nonlinear optics, quantum optics and high-power optics led to a total revolution in telecommunications, medicine, spectroscopy and weaponry. Additionally, lasers are now being considered for wireless power transmission, propulsion, and space exploration. The fast increase of the commercial business of fiber lasers was worth over 2.17 billion dollars in 2020 and now in 2021, it is expected to reach 2.36 billion dollars at a compound annual growth rate (CAGR) of 8.8%, which is the maximum value among other lasers technologies [1]. With the recovering from covid-19, it is expected that fiber laser market reaches 3.4 billion dollars by 2025 at a CAGR of 9.6%.

Cubesats are also shifting the engineering paradigm and space exploration in the last years, in various areas such as multimedia communications, data distribution, telephone and television, transportation and logistics, weather information and climatic research, navigation, safety, security, and rescue. This field is identified as an imminent and promising technological market. The predictions say market size is expected to grow from 2.3 billion dollars in 2021 to 5.7 billion by 2026, with a CAGR of 20.4% between 2021 and 2026 [2]. The energy demand in this market segment has also increased dramatically due to the huge progress in CubeSat technologies, requiring larger deployable solar arrays, lower power electronics, efficient energy storage systems and further energy transfer/harvesting systems.

For all the above mentioned, WiPTherm was born. It consists of a European project

that aims to design, implement and develop an inventive Wireless Energy Transfer system, capable of charging the energy storage system used in CubeSat technologies. The technology consists of a clean solution for energy transfer. The energy harvesting system comprises dozens of microarrays of 2D thermoelectric generators, resulting in a photo-thermoelectric plasmonic (HPTP) system that has the ability to convert photons' energy into electrical energy, via thermal gradient [3]. The wireless thermal stimulation will be performed through a large-range high-power laser beam capable of operating at large distances. A scheme of the full system can be perceived in figure 1.1.

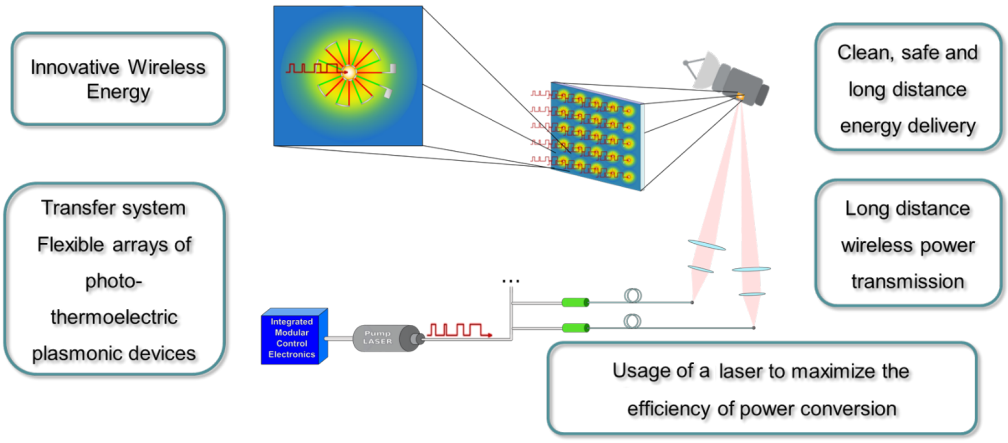



FIGURE 1.1: Concept of WiPTherm project [4].

The main mission at our institute, INESCTEC, is to develop the high-power laser system, capable of operating at large distances, and the optical system that will shape the beam so it will meet the requirements when arriving at the CubeSat. This dissertation work is inside the Work Package 4 in figure 1.2 and the development of this high power fiber laser is taking place at INESCTEC.

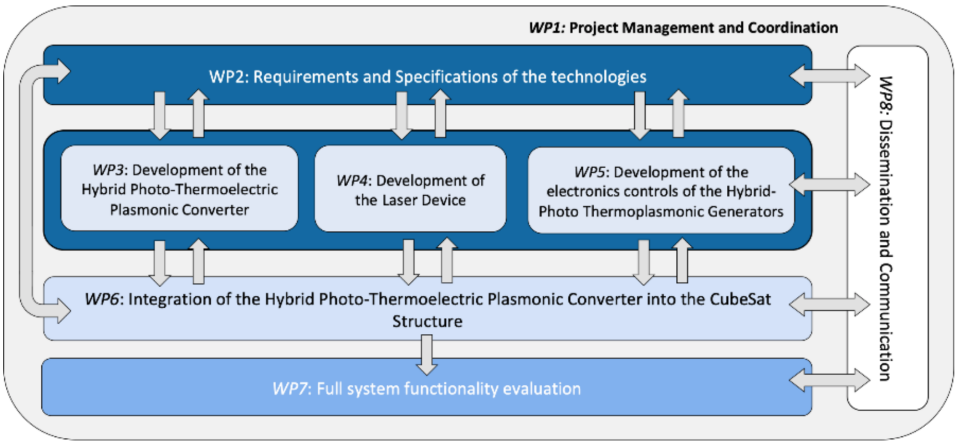



FIGURE 1.2: WiPTherm project Work Packages description [4].

## 1.2 Objectives

The aims of this thesis are the study and compilation of the fundamental concepts and state of the art relevant for the development of the high power fiber laser, as well as performing a preliminary work that motivates the topic such as simulation of turbulent atmospheric propagation and beam expansion calculation.

The dissertation final goal is to size and integrate optical components harmoniously to obtain a fiber laser that accomplishes high continuous-wave (CW) output power. It is also important that the final source is stable, with a monomode emission, and with an optical output power exceeding 15 $W$. The optical components of the final setup should be tuned so it is produced a collimated output beam.

## 1.3 Document Structure

The chapters are organized as follows:

- Chapter 1 - This first chapter introduces the context and motivation for this dissertation;
- Chapter 2 - In this chapter, the fundamental knowledge about lasers and some applications is exposed;
- Chapter 3 - Here is a summary of the most relevant prior art and approaches to fiber lasers and high-power lasers.
- Chapter 4 - It is detailed the preliminary work on the expansion of the beam for 1 $m$, 1 $km$ and 500 $km$ and its turbulent atmospheric propagation
- Chapter 5 - The fiber laser design and its characterisation are presented.

## 1.4 Outputs

During this thesis, one poster was presented at the international conference Optics and Photonics for Scientific Progress (OPSP) at the University of Kent in the UK. Another poster was presented in the Doctoral Congress in Engineering in the Faculty of Engineering of the University of Porto while being a junior collaborator at INESCTEC. Two oral presentations took place: one at IJUP, a conference for young researchers of the University

of Porto; and another at the Faculty of Sciences of the University of Porto for Physics and Engineering Physics students.

Here are the references of the respective articles:

1. Fernando Maia, Paulo Robalinho e Orlando Frazão, Simulations of atmospheric propagation under turbulent conditions and high power fiber laser, OPSP- Optical Conference for Scientific Progress, University of Kent, April, 2021.

2. Fernando Maia, Paulo Robalinho e Orlando Frazão, Simulating the propagation of a laser through turbulent atmosphere, DCE- Doctoral Congress in Engineering, fourth edition, FEUP - Faculty of Engineering of the University of Porto, June, 2021.

3. Fernando Maia, Paulo Robalinho e Orlando Frazão, High Power Fiber Laser for Space Applications, IJUP- Encontro Investigação Jovem, 14ª edição, May, 2021.

# Chapter 2

# Lasers' Fundamentals

## 2.1 Introduction

It all began in 1863 when Maxwell invoked the four commandments that govern Electrodynamics [5], which are present in equation 2.1*.

$$\begin{aligned} \nabla \cdot \mathbf{D} &= \rho \\ \nabla \cdot \mathbf{B} &= 0 \\ \nabla \times \mathbf{E} &= -\tfrac{\partial \mathbf{B}}{\partial t} \\ \nabla \times \mathbf{H} &= \mathbf{J} + \tfrac{\partial \mathbf{D}}{\partial t} \end{aligned} \tag{2.1}$$

These four equations are known as Maxwell's equations, and they summarize the entire theoretical content of Classical Electrodynamics.

In free space, these equations simplify setting $\rho = 0$ and $\mathbf{J} = 0$. Hence the result is a set of coupled partial differential equations of first order for $\mathbf{E}$ and $\mathbf{B}$. One can decouple, for example, the $\mathbf{E}$ part [6], and applying the operation $\nabla \times (\nabla \times \mathbf{E})$ one obtains:

$$-\frac{\partial}{\partial t}(\nabla \times \mathbf{B}) = -\mu_0 \epsilon_0 \frac{\partial^2 \mathbf{E}}{\partial t^2} \tag{2.2}$$

and we get the expression of equation 2.3 where $c$ is the velocity of the wave in vacuum $c = \frac{1}{\sqrt{\epsilon_0 \mu_0}}$. This equation is known as the wave equation for the $\mathbf{E}$ field.

$$\frac{\partial^2 \mathbf{E}}{\partial z^2} - \frac{1}{c^2}\frac{\partial^2 \mathbf{E}}{\partial t^2} = 0 \tag{2.3}$$

On the other hand, when a wave propagates inside a non magnetic medium with no free charges, $\rho \neq 0$, the equation 2.3 needs to be modified. The wave equation is very

*the bold letters represent vectors.

similar to the wave equation in free space, but it has an additional term, that can be seen in equation 2.4.

$$\frac{\partial^2 \mathbf{E}}{\partial z^2} - \frac{1}{c^2}\frac{\partial^2 \mathbf{E}}{\partial t^2} = \mu_0 \frac{\partial^2 \mathbf{P}}{dt^2} = \mu_0 N q \frac{\partial^2 \mathbf{r}}{dt^2} \tag{2.4}$$

The term on the rightmost side tells us a very important thing: light can be produced by accelerated charges! The most known forms of sources of light are: the synchrotron radiation (light emitted by charged particles), molecular, atomic or nuclear transitions and particle-antiparticle annihilation (e.g. electron-positron interaction, which generates two photons of gamma radiation) [5].

Most of the light produced in the Universe comes from atomic and molecular vibrations. For example, electrons oscillate around nuclei at "high" frequency: $\approx 10^{14}$ to $\approx 10^{17}$ cycles per second $(Hz)$; molecule nuclei vibrate relative to each other with a "intermediate" frequency: $\approx 10^{11}$ to $\approx 10^{13}$ $Hz$; rotation of the molecules' nuclei at "low" frequency: $\approx 10^{9}$ to $\approx 10^{10}$ $Hz$.

Our knowledge of nature largely comes from information that reaches us in the form of electromagnetic radiation. This radiation extends over the entire spectrum. A representation of the light spectrum can be seen in figure 2.1. It can be noted that the energy of a wave depends on its wavelength (or frequency).

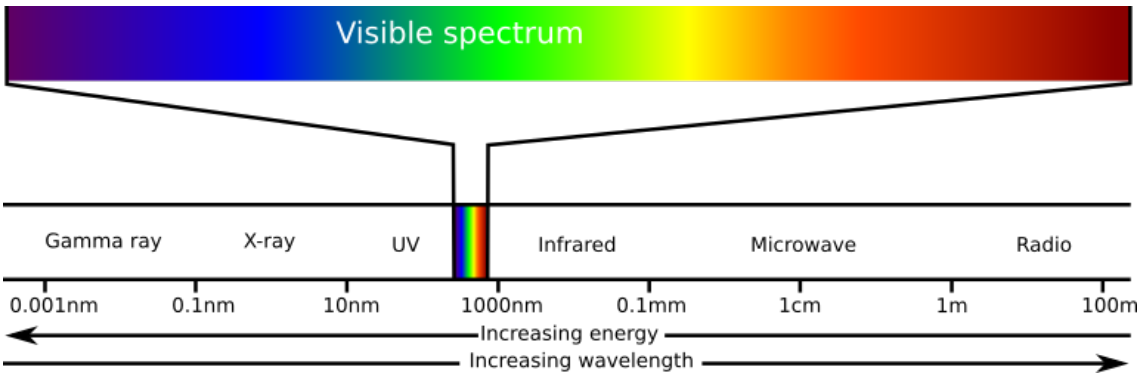



FIGURE 2.1: Scheme of the electromagnetic spectrum [7].

To discover the laser it was necessary to understand the fundamental physical processes responsible for the emission of this radiation.

## 2.2 Laser Technology

### 2.2.1 Working principles

LASER is an acronym for Light Amplification by Stimulated Emission of Radiation and now it is also a word. To explore this topic, we will go back to 1917 and meet a unique scientist called Albert Einstein. He needs no introduction, but interestingly one of the most elegant and modest works he did was the foundation of the LASER's theory: the "Zur Quantentheorie der Strahlung", or in English "On the quantum theory of radiation" [8].

To understand the three fundamental processes in that paper, firstly one will consider an atom (or molecule) with two levels of energy, the fundamental (1) and an excited one (2), with respective energies $E_1$ and $E_2$, where $E_1 < E_2$. Because $E_1 < E_2$ the atom tends to decay to level 1. The energy released by the atom corresponds to the difference of energy $E_2 - E_1$. If this energy is released in the form of an EM wave, the process is called Spontaneous (or radiative) Emission. The frequency associated with this process is given by:

$$v_0 = \frac{(E_2 - E_1)}{h} \tag{2.5}$$

This energy can also be expressed as a non-radiative decay. For instance, the decay can occur in an internal/kinetic energy transfer process to the surrounding atoms or molecules.

Now, one can consider an atom initially in level 2 and an EM wave with frequency $v = v_0$ (equal to the spontaneous emission) reaching on it. There is a finite probability that the incident wave forces the transition from level 2 to level 1 [9] and in this case, the energy $E_2 - E_1$ is emitted in the form of an EM wave that adds (coherently) to the initial wave, and so there is light amplification. To this process, Einstein called Stimulated Emission. The Absorption happens when an incident EM wave has at least frequency $v = v_0$: there is a finite probability of the atom jumping from level 1 to level 2.

In figure 2.2 one can see the illustration of these three processes. The sub-figure (a) shows the decay of the excited level 2 to level 1 with an energy release of $hv = E_2 - E_1$, the so-called spontaneous emission. Sub-figure (b) shows us that an incident photon can cause a transition from level 2 to level 1 emitting an EM wave that sums to the initial

wave, the process called stimulated emission. Last but not least, sub-figure (c) shows the level rise from level 1 to level 2 with the absorption of $hv = E_2 - E_1$.

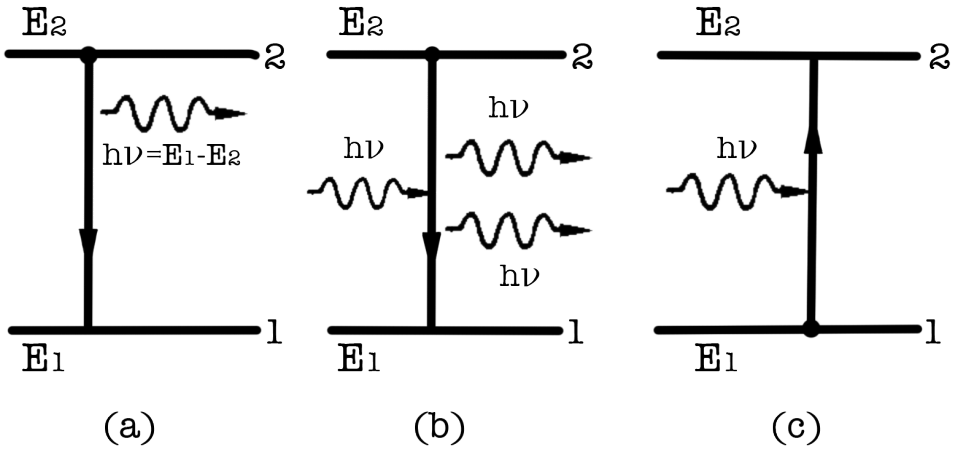



FIGURE 2.2: Schematic illustration of the three processes: (a) spontaneous emission, (b) stimulated emission, (c) absorption.

Usually, absorption occurs because the atoms are in the fundamental state. If more atoms live in the excited state, compared to the fundamental state, we can have amplification instead of absorption, and that is called population inversion.

A system of 2 levels follows the Boltzmann distribution equation:

$$\frac{N_2}{N_1} = e^{-(E_2 - E_1)/kT} \tag{2.6}$$

where $N_1$ is the population of level 1 (atoms or molecules per unit volume) and $N_2$ is the population of level 2. In thermal equilibrium, inversion is impossible. Only when $N_2 > N_1$, the material act as an amplifier. Einstein showed us that "when light strikes a set of atoms, stimulated emission and absorption are equally likely" [8]. It is immediately evident that such a system of 2 levels would not work (at least in the steady-state). When the condition $N_2 = N_1$ is reached, the stimulated emission will compensate the absorption and vice versa, reaching the two level saturation.

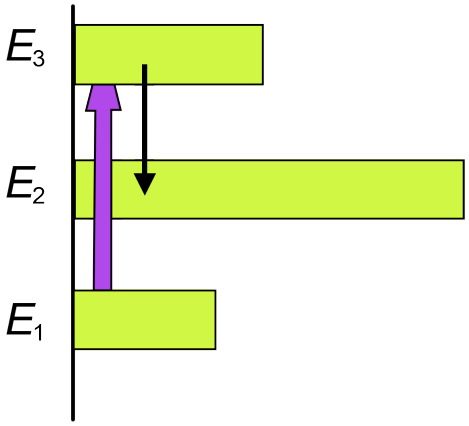



FIGURE 2.3: Scheme of a 3 level laser.

Consequently, it is needed at least a 3 level system, presented in figure 2.3. The medium is pumped and the atoms are raised from the ground level 1 to level 3, and then quickly decay (non-radiatively) to level 2. The population inversion is now achieved between levels 2 and 1 and we now have light amplification by stimulated emission of radiation (LASER).

To build a laser system, one needs an active medium where amplification can take place. To pump the active medium and achieve the population inversion one also needs a source of energy, and that can be a lamp, a laser or an electrical power supply. In figure 2.4 it is presented a simple laser scheme.

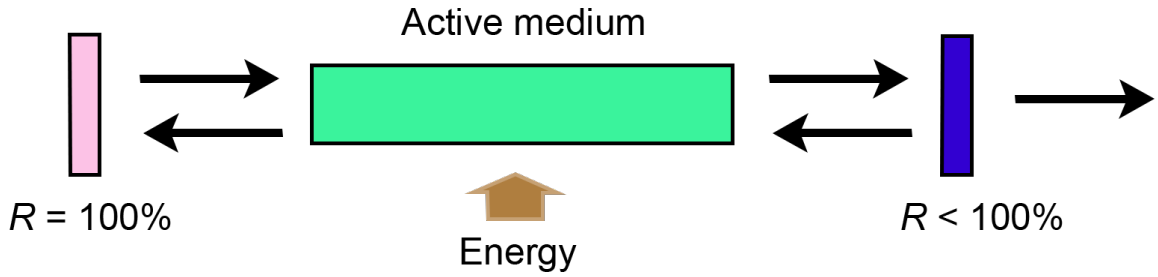



FIGURE 2.4: Laser cavity scheme.

The active medium is placed between two mirrors, one with a reflectivity of 100% and another one with a reflectivity somewhere between 99% and 100%. The main idea is to have a beam bouncing back and forth between the two mirrors and being amplified in the active medium (a resonant cavity). The output of the laser is the mirror with lower reflectivity.

### 2.2.2 Groundbreaking work using lasers

In 1955, James P. Gordon and H. J. Zeiger and Charles H. Townes achieved a MASER (microwave amplification by stimulated emission of radiation) oscillation with a system using vapour [10], producing extremely monochromatic and coherent light, reaching frequencies in the gigahertz order. Three years later, A.L.Schawlow and Townes showed (in theory) that by using a resonant cavity, having many resonant modes, maser oscillation at the infrared and optical region wavelengths can be achieved by pumping an atomic potassium gas with reasonable amounts of incoherent light [11]. The work of Charles H. Townes, Nicolay G. Basov and Aleksandr M. Prokhorov was worth a Nobel prize in 1964 "for fundamental work in the field of quantum electronics, which has led to the construction of oscillators and amplifiers based on the maser-laser principle" [12].

Theodore Maiman, in 1960, produced a short pulse of coherent light from his device [13]. In figure 2.5 one can see how the first laser was built: a quartz flash lamp is pumped with an electrical discharge from the power supply. Then, the flash produced in the quartz lamp pumps the ruby crystal and the cavity produces a pulse of laser light, this time a visible one with $\lambda \approx 694\ nm$.

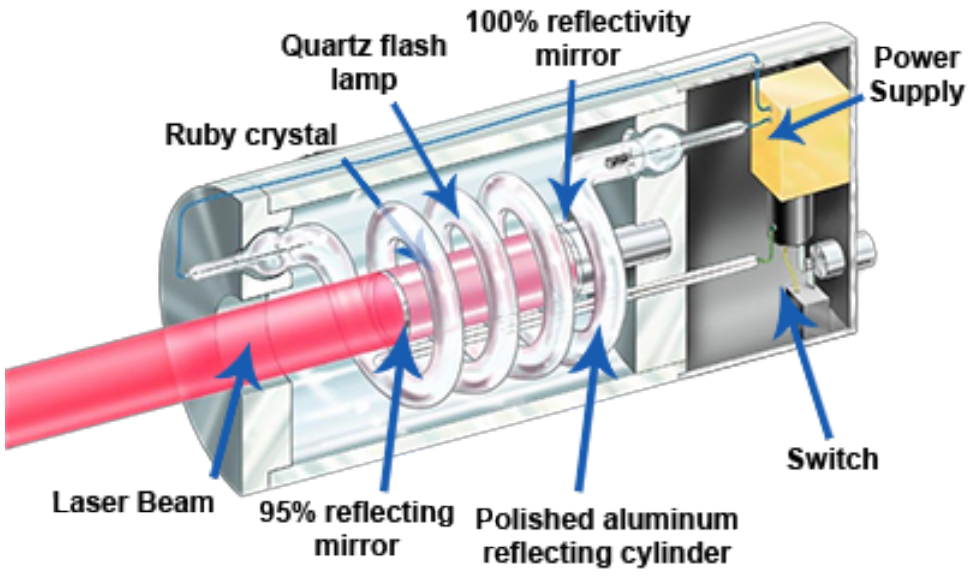



FIGURE 2.5: First working laser - by Theodore Maiman [14].

Maiman's humble device literally changed the world. Other variety of lasers appeared over the years, such as the carbon-dioxide laser [15], the ion laser [16] and the helium-neon laser [17, 18], dye laser [19], the free-electron laser [20], metal-vapour laser [21], the

semiconductor laser [22] and the excimer laser [23, 24].

Laser light technology, characterized by a well directional, coherent and intense light beam, led to several Nobel prizes: the previously mentioned discovery of the Maser by Charles H. Townes, Nicolay G. Basov and Aleksandr M. Prokhorov [12], in 1964; the invention of Holography by Denis Gabor [25], in 1971; the development of laser spectroscopy by Nicolaas Bloembergen and Arthur Leonard Schawlow [26], in 1981; the invention of the hydrogen maser as an atomic clock by Norman F. Ramsey [27], in 1989; the development of methods to cool and trap atoms with laser light by Steven Chu, Claude Cohen-Tannoudji and William D. Phillips [28], in 1997; the hetero-junction semiconductor devices (semiconductor lasers) by Zhores I. Alferov and Herbert Kroemer [29], in 2000; the discovery of the "fifth state of matter", the Bose-Einstein condensate by Eric A. Cornell, Wolfgang Ketterle and Carl E. Wieman [30], in 2001; the development of laser-based precision spectroscopy by John L. Hall and Theodor W. Hänsch and the contribution to the quantum theory of optical coherence by Roy J. Glauber [31], in 2005; the discovery of the blackbody form and anisotropy of the cosmic microwave background radiation using the masers from the COBE satellite by John C. Mather and George F. Smoot [32], in 2006; the achievements concerning the transmission of light in fibers for optical communication by Charles Kuen Kao, in 2009; and last but not least, Arthur Ashkin was awarded for the optical tweezers and their application to biological systems, and Gérard Mourou and Donna Strickland "for their method of generating high-intensity, ultra-short optical pulses.", the chirped pulse amplification [33], in 2018.

The list of laser applications keeps growing. In medicine, lasers are used to perform surgery, for example, eye surgery with a femtosecond laser, and they are also used to diagnose diseases (optical coherence tomography [34], laser microscopy [35], isotope production [36], along with others). Regarding the heavy industry, lasers are revolutionizing the paradigms of welding, cutting, marking, cleaning, and micro-machining [37]. Sensors and weaponry in the defence context are also areas where lasers play an important role. In the entertainment/information technology world, the presence of lasers is abundant. They are present on CD technology, DVD, Blu-ray, barcode readers, and others. Lasers are also used for communications (communication between satellites, fiber optics, inter-chip communication). In all research areas of the natural sciences and medicine, lasers are widely used, and in particular, in a very special area called extreme physics: particle acceleration [38], X-ray production [39], inertial confinement fusion (ICF) [40], and others.

Laser technology is also used in extreme physics: high-precision frequency measurements [41], optical clocks (as mentioned before), etc. These are just some of the numerous applications of lasers that exist today.

### 2.2.3 Fiber lasers - an introduction

Fiber lasers are generally lasers that use optical fibers as the gain medium. Usually, the active medium is a fiber doped with rare-earth ions such as neodymium ($Nd^{3+}$), ytterbium ($Yb^{3+}$), erbium ($Er^{3+}$), thulium ($Tm^{3+}$), among others [42]. There is then one or more pumping lasers that will supply enough energy to the active medium to have population inversion. These pumping lasers are mostly diode lasers.

Recalling the picture in the figure 2.4, we already have the pumping (energy), but the cavity (resonator) is missing. There are several possibilities. For commercial lasers, it is common to use Bragg fiber gratings instead of mirrors, made directly on the doped fiber [42]. These gratings are a periodic variation of the refractive index in the core of an optical fiber.

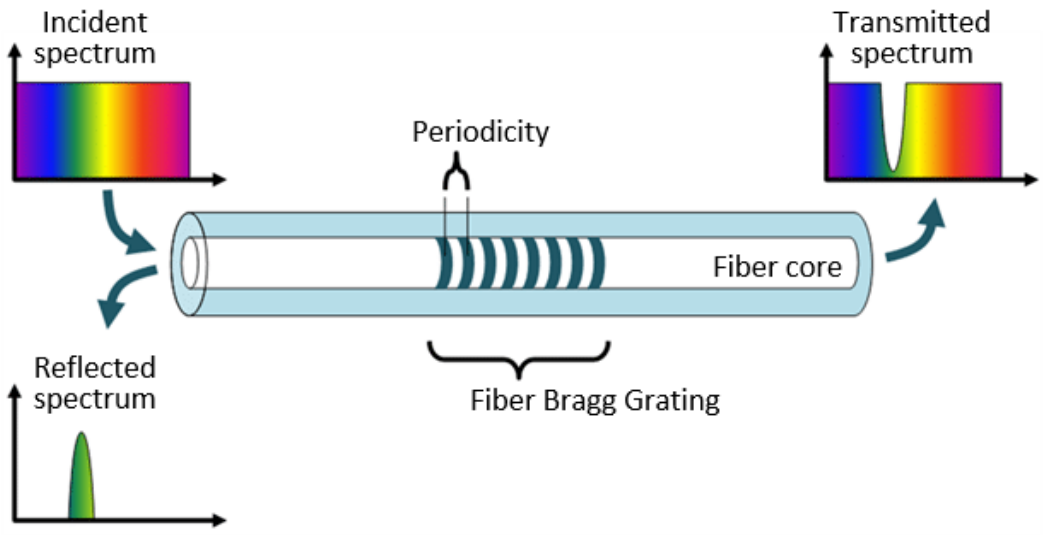



FIGURE 2.6: Fiber grating scheme [43].

In figure 2.6 one can see a Fiber Bragg Grating (FBG), and if a broadband spectrum enters the fiber, the grating will reflect in a specific wavelength. With a sufficient number of periodic perturbations in the fiber, the reflection can be very optimised for a particular

wavelength $\lambda = 2n_{eff}\Lambda$ , where $n_{eff}$ is the effective refractive index of light in the fiber and $\Lambda$ is the grating period. These FBGs can be arranged as a set of two, one at each end of the active medium (doped fiber), so that there is a cavity in the centre, as shown in the figure 2.7.




FIGURE 2.7: Fiber grating cavity scheme [44].

Most fiber lasers are pumped with one or more diode lasers [45]. This pump light can be inserted right into the core, or into the cladding. In figure 2.8, one can see a setup of a cavity composed of a doped fiber, two dichroic mirrors (that only reflects the laser wavelength), two lenses to focus the beam inside the fiber and to collimate the beam after the fiber. Because of the beam large area, the intensity on the mirror is reduced and the surface may have a smooth reflection, without being damaged. This setup is highly sensitive, very susceptible to misalignment that can cause losses.

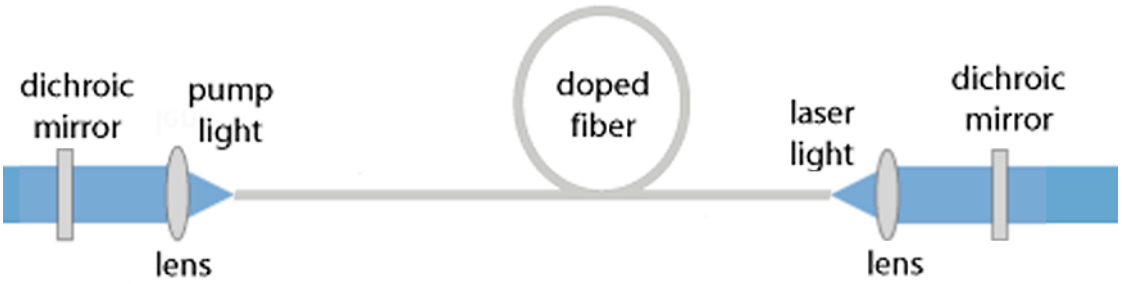



FIGURE 2.8: Simple fiber laser scheme [46].

In this chapter, we have just flown over some of the most important principles of lasers, such as stimulated emission, absorption and spontaneous emission. We also had the opportunity to see how a 3-level system works. We also analysed the structure of a typical laser cavity. Numerous examples of laser applications and innovative work were presented. And, last but not least, we analysed the case of fiber lasers, seeing their basic working mechanisms. In the next chapter, a brief review of fiber lasers is presented.

# Chapter 3

# Fiber Lasers - A Brief Review

## 3.1 A Brief Review

It all began with the discovery already mentioned in the previous chapter: in 1960, Theodore Maiman invented and constructed the very first laser, a ruby laser [13]. Four years of development later, the first fiber laser appeared [47]. It was a neodymium-doped silica fiber cladding-pumped by a flash tube with an emission around 1.06 $\mu m$. Subsequently, different doping elements popped up such Erbium at 1.5 $\mu m$ [48], Ytterbium centered at 1 $\mu m$ [49], Thulium at 2 $\mu m$ [50], Dysprosium 3 $\mu m$ [51], Praseodymium centered around 491 $nm$ and 635 $nm$ [52] and also Holmium at 2.1 $\mu m$ [53]. From all of these dopants, Erbium allowed the fiber technology to revolutionize the area of optical telecommunications: on one hand, the low losses at 1.5 $\mu m$ led to large distances data transference; on the other hand, the large gain band ($\Delta\lambda \sim 100\ nm$) grants wavelength multiplexing - amplification of multiple data channels with high data rates without detrimental distortions due to gain narrowing [54].

At the dawn of the laser era, fiber's doped cores were pumped, so the pump and the amplified signal travelled together inside it. However, there were some limitations: to keep a transverse single-mode laser emission it was necessary small values of core size and Numerical Aperture ($NA$), forcing a single-mode pumping diode to be used. Despite the progress made in recent years, single-mode semiconductor diodes only provide up to few watts thus limiting the output powers of fiber laser sources. To overcome this limitation, Snitzer et al. developed an elegant concept of double-clad fiber [55], supported on the original idea of Maurer, in 1974 [56]. In a double-clad fiber, the signal is guided inside

the core while the pump propagates through an inner cladding with higher dimensions and $NA$. In figure 3.1 one can see a schematic representation of a double-clad laser.

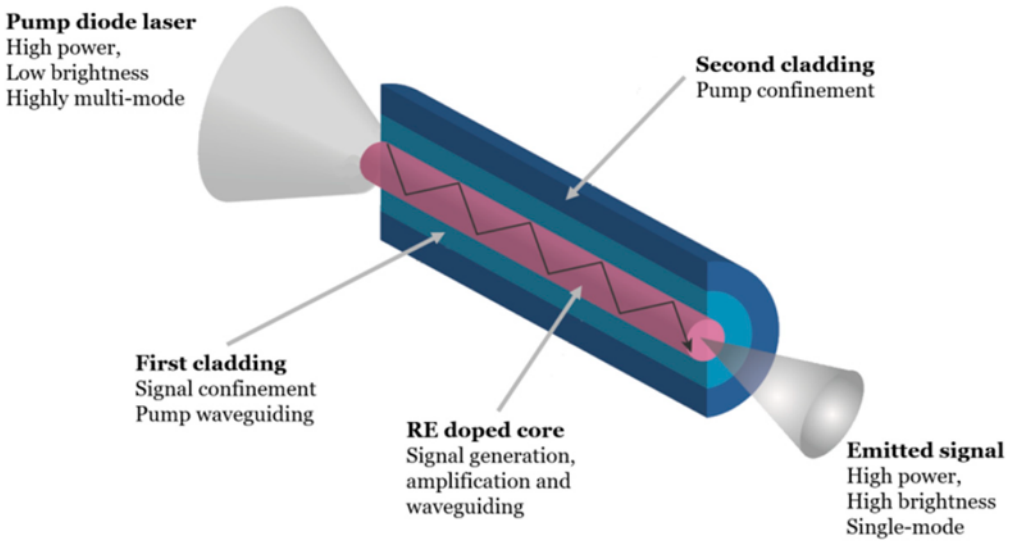



FIGURE 3.1: Schematic representation of a double-clad fiber [57].

The inner cladding high $NA$ number can be assured by doping it with fluorine. The outer cladding can even be air (air cladding), thus the low index. The refractive index of the outer cladding is far lower than the one of the inner cladding, whose index is itself lower than the core [57]. A few hundred micrometers is a typical dimension for the inner cladding and its $NA$ can fluctuate between 0.2 and 0.9 depending on the outer cladding's proprieties. Due to their higher dimensions and since $NA$ is proportional to the sine of the angle of acceptance of the guided light, double-clad fibers allow efficient coupling of light provided by high power multi-mode pumping diodes delivering up to a few hundred watts and even kilowatts. Therefore, double-clad fiber lasers convert the power of multi-mode pump diode lasers into a single transverse mode emission. This double-clad fiber geometry technology paved the way for the research of high power laser sources, now largely used over the world for high power applications.

With power scaling, other nonlinear effects such as stimulated Raman scattering and stimulated Brillouin scattering began to limit fiber technology. To overcome this second limitation, the solution had been to increase the core size leading to Large Mode Area (LMA) fibers [58]. Applying a bending radius [59], selective signal launching [60], gain filtering [61] and other as well as fiber structures such as depressed-index core [62], tapered fiber [63] and photonic crystal fibers [64] were studied and developed to reach the

highest core dimensions possible while maintaining a transverse single-mode emission allowing high energies and high peak powers. At the moment, with CPA, it is possible to make a 38 $GW$ peak power source with a core diameter of 105 $\mu m$ for an active micro-structured fiber [65]. As a comparison, core diameters of telecom fibers barely exceed 9 $\mu m$.

Nowadays, the highest average output power fiber lasers are doped with Ytterbium [66]. These ions in a silica host possess an emission cross-section centered around 1030 nm and spanning from 980 to 1100 nm [67], as well as an absorption cross-section maximum around 915 nm and 976 nm. Over the last decade, developments have been extensively made on high-power semiconductor diodes emitting at these wavelengths and now kW-class diodes are commercially available. Furthermore, due to the lifetime of the metastable state of 1 $ms$ and a quasi-two-level energy scheme, high doping concentrations are allowed, leading to short fiber lengths due to high pump absorption [68]. The Ytterbium ion has low quantum defects, so efficiencies can reach the value of 90% [69]. Currently, the most powerful Yb-doped fiber laser source is commercialized for industrial applications, providing an average output power up to 100 $kW$ with an efficiency of 35% but, unfortunately, it is multimode, which means that the emitted beam is highly divergent and its brightness is not optimal [70]. IPG Photonics, the same company of these 100 $kW$ multi-mode fiber laser also offers a transverse single-mode version able to deliver 10 $kW$ of average power.

### 3.1.1 Atmospherical considerations

Even though Yb-doped fibers have attractive features due to their performances, in the context of this thesis these may not be the best, considering the propagation losses due to atmospheric transmission. The ultimate goal is to reproduce the same results at 500 $km$ from Earth ground, and the Cubesat would be in orbit. One can think of some obstacles to the realization: the propagation losses and profile distortion due to atmospheric transmission are almost negligible at 850 $m$ but at 500 $km$ they must be taken into account. For this reason, it is necessary to choose an adequate wavelength emission. In a first simple approach, it is studied the atmospheric transmittance of the light coming from the sun. Since the sun can be considered a black body, its spectral radiance can be easily determined from its temperature. After analyzing sunlight transmitted to Earth's ground,

it becomes possible to deduct the atmospheric transmittance as a function of the wavelength. A typical curve of the atmospheric transmittance was realized by J. A. Shaw et al. using Modtran5 software [71]. Analysing the data from it and in particular the region near 1 $\mu m$, it follows that this same region is not ideal, so the use of Yb-doped fiber can't be used for the project. Another interesting window would be, for instance, around 3.5 $\mu m$, but there's a lack of laser sources in this wavelength. This reduces the possibilities to two intervals, one around 1.6 $\mu m$ and the other around 2 $\mu m$, since they seem to have the highest transmittance through the atmosphere and match well with emission cross-sections of two rare-earth dopants: Erbium and Thulium respectively.

Thulium's popularity has grown in recent years due to its emission band, from 1.7 $\mu m$ to 2.1 $\mu m$, which is quite interesting to generate new wavelengths in the middle infrared region by non-linear conversion [72]. Generally pumped at 790 $nm$, the quantum defect should limit the efficiency at a maximum of 40% when emitting at 2 $\mu m$ but thanks to the cross-relaxation, process implying energy transfers between ions in the silica host, it becomes possible to reach efficiencies as high as 75% [73]. However, fiber and optical components around 2 $\mu m$ are scarce. For this reason, erbium-doped fibers were chosen in the first approach for the application in the WiPTherm project.

There is a large commercial availability of optical and fiber components around 1.5 $\mu m$ as well as a real technological maturity of erbium-doped fibers owing to their extensive development for optical telecommunication making their integration within simple all-fibered laser architectures easily achievable.

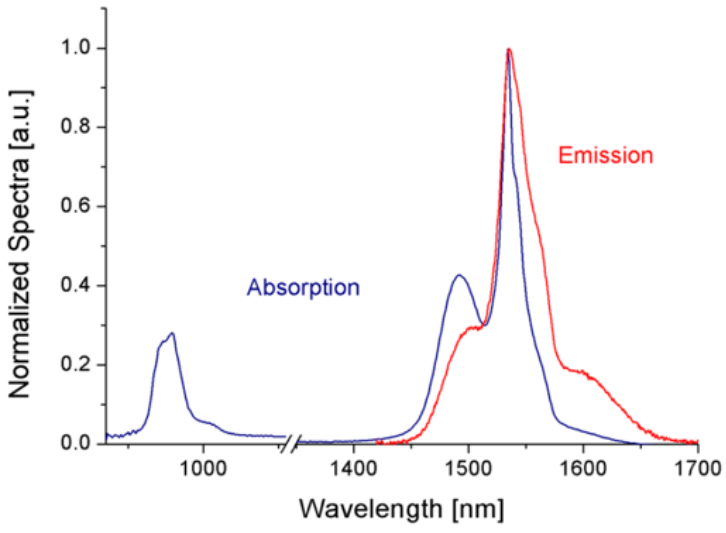



FIGURE 3.2: Typical absorption and emission spectra of Erbium ions [74].

The downside of Erbium-doped fibers is the fact that they do not support high rates of Er ions doping due to the quenching phenomenon which strongly reduces efficiency by increasing losses on the signal in the fiber core [75]. In figure 3.2, one can see that the absorption of Erbium ion is centered around 980 $nm$ and 1500 $nm$, while emission occurs between 1.5 and 1.7 $\mu m$. Pumping around 980 $nm$ will highlight the quantum defects, limiting the output. Added to that, the absorption cross-section around 980 $nm$ is pretty low, so it is required a significant Er-doped fiber length to correctly absorb the pump power. Nevertheless, efficient ($\sim$ 40%) and high power laser sources ($>$ 70$W$) had been realized with Erbium-doped fiber [76] pumped at 976 $nm$. To increase the efficiency and/or shorten the fiber length, co-doping Erbium with Yb ions had also been studied.

In addition to greatly increasing pump absorption at 976 $nm$, the co-doping implies an energy transfer from Yb ions to Er ones leading to an increase of lifetime in Er:Yb doped fibers [77]. Output powers higher than 150 $W$ were demonstrated with Er:Yb doped fiber laser sources [78, 79]. One aspect that one must consider when increasing pump power is the amplified spontaneous emission (ASE) around 1030 $nm$ due to Yb ions, which limits power scaling. ASE appearance can however be mitigated [80, 81]. Another solution to significantly increase output average powers and efficiency is the in-band pumping (also named resonant pumping), which consists in pumping at a wavelength where ground state absorption exists (for Erbium these wavelengths are 1.48 $\mu m$ and 1.53 $\mu m$, seen in fig 3.2).

## 3.2 Concluding Remarks

Regarding this brief review, let us resume the laser source requirements for this dissertation. The objective will be to realize an efficient Erbium-doped fiber laser source potentially able to deliver more than 15 $W$ of average output power in continuous-wave operation. The laser emission has to be centered around 1.5 $\mu m$ to 1.6 $\mu m$ bearing in mind the atmospheric transmission and diffraction-limited (single-mode) to minimize beam divergence. Since only continuous-wave operation is required, a complex LMA structure is not required. The fiber will be realized by the University of Limoges group with REPUSIL sintering powder technology [82], which is particularly well mastered in their lab [83, 84]. Finally, one must consider the proper setup for the fiber laser depending on the way we want to design CW signal emission either in a simple all-fiber architecture

with Fiber Bragg gratings acting as end mirror and output coupler, or in a more complex Master Oscillator Power Amplifier (MOPA) architecture.

# Chapter 4

# Beam Propagation Analysis

## 4.1 Natural divergence of a Gaussian beam

### 4.1.1 Theoretical principles of divergence

In paraxial approximation, if one wants to know a profile at one plane $u(x, y, z)$, knowing the previous profile $u(x_1, y_1, z_1)$, we do a superposition of all individual wavelets emitted from plane $z_1$, which is the same of evaluating the integral in equation 4.1 [85].

$$u(x, y, z) = \frac{1}{B\lambda} \iint u\left(x_1, y_1, z_1\right) \exp -jk \left[ \frac{A\left(x_1^2 + y_1^2\right) + D\left(x^2 + y^2\right) - 2x_1 x - 2yy_1}{2B} \right] dx_1 dy_1 \tag{4.1}$$

Equation 4.1 considers wave propagation, within the paraxial approximation, through a general optical system described by the ABCD matrix [86]. It is a result of the famous Huygens-Fresnel-Kirchoff integral in the so-called Fresnel approximation. The field at the new plane is obtained by the superposition of the individual wavelets emitted from a plane and transmitted through this system.

If one consider Gaussian beam propagation $u(x, y, z) \propto \exp -jk \left[ \left(x^2 + y^2\right) / 2q \right]$ we will get the equation 4.2.

$$q = \frac{Aq_1 + B}{Cq_1 + D} \tag{4.2}$$

The equation 4.2 is able to compute $q$ parameter in $z$ plane knowing the $ABCD$ matriz inherent to the propagation medium and the $q_1$ parameter in $z_1$ plane [85]. One can take

a closer look at the $q$ parameter: $\frac{1}{q} = \frac{1}{R} - j\frac{\lambda}{\pi w^2}$ . The real part corresponds to the radius of curvature of the wave and the imaginary part is related to the beam waist $w$.

In free space propagation, $A = D = 1$ and $B = z$, and from equation 4.2 we get:

$$q = q_1 + z \tag{4.3}$$

Assuming that we have a plane wave, $R = \infty$, at the waist $z = 0$ :

$$(1/q_1) = -j\left(\lambda/\pi w_0^2\right) \tag{4.4}$$

where $w_0$ is the spot size at $z = 0$.

Manipulating equation 4.2 and 4.4 it is found equation 4.5 predicts the value of a Gaussian beam waist $w_1$ at a plane $z$, knowing the initial waist $w_0$ [85].

$$w_1(z) = w_0^2\left[1 + \left(\frac{\lambda z}{\pi w_0^2}\right)^2\right] \tag{4.5}$$

This waist $w_1$ used represents the distance to the $z$ axis for which the value of the electric field on that same axis falls to $1/e$, and therefore the diameter is $2w$.

### 4.1.2 Waist prediction

We used equation 4.5 to study the behaviour of the waist. We are interested in the expansion for our lab experiment, a propagation of 1 $m$, and also interested in the project prototype for 1 $km$. Furthermore, we are curious about the ultimate goal propagation of 500 $km$, an orbital distance.

In figure 4.1 (a), one can see the final waist of the beam, $w_1$, as a function of $w_0$ for a 1 $m$ propagation. For different initial waists $w_0$ we get different values of the final waist $w_1$ and it was possible to detect a minimum for $w_1$. In the subfigure (b) is represented the pairs $w_0$ and the correspondent minimized $w_1$, function of the distance. The values of the final waist $w_1$ are the minimum possible considering natural divergence. If we trace a vertical line we can found the minimizer $\iff$ minimum pair $w_0 \iff w_1$, for a certain propagation distance.

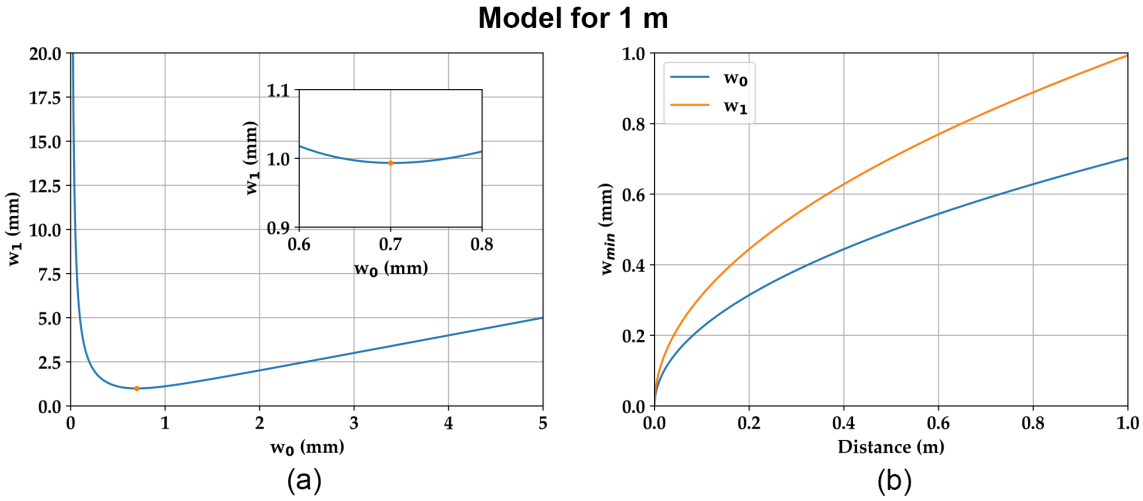



FIGURE 4.1: Model for 1 $m$: (a) minimization of $w_1$, (b) $w_{min}$ function of the distance.

Figure 4.2 is analogous to figure 4.1, but now the analysis is done for a propagation distance is 1 $km$ instead of 1 $m$. In (a) one can see the final waist $w_1$ as a function of $w_0$ for 1 $km$ propagation and, in the subfigure (b) is presented an extension of (b) from figure 4.1. One can see that for 1 $km$ propagation, the smallest waist that can be achieved is one order of magnitude bigger than the minimum waist for 1 $m$ propagation.

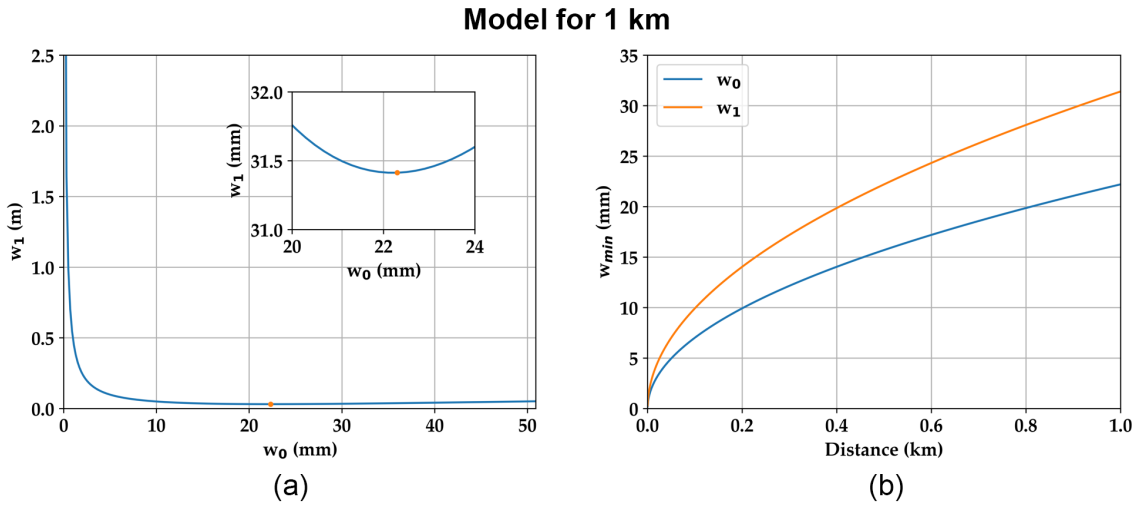



FIGURE 4.2: Model for 1 $km$: (a) minimization of $w_1$, (b) $w_{min}$ function of the distance.

In (a) of figure 4.3 one can see again $w_1$ function of $w_0$ but this time for 500 $km$, which is the typical altitude for CubeSats. As we can conclude, it is needed an initial waist of 0.496 $m$ to minimize the final waist! So the optical components must be relatively big to achieve $w_1 = 0.702\ m$ at the end of the $500km$ propagation. Typically, we need to have a diameter of the optical components much larger than 2w to harness the full Gaussian

beam, i.e. about $6w$ will be the minimum, which means we should have a size of about 3 meters for the optical components of a ground station. Having a final waist $w_1 = 0.702\ m$ is a fact that needs to be taken into account when we have a target of an effective area of $0.3\ m \times 0.4\ m$. Subfigure (b) of figure 4.3 is an extension of (b) of figure 4.1 and 4.2.

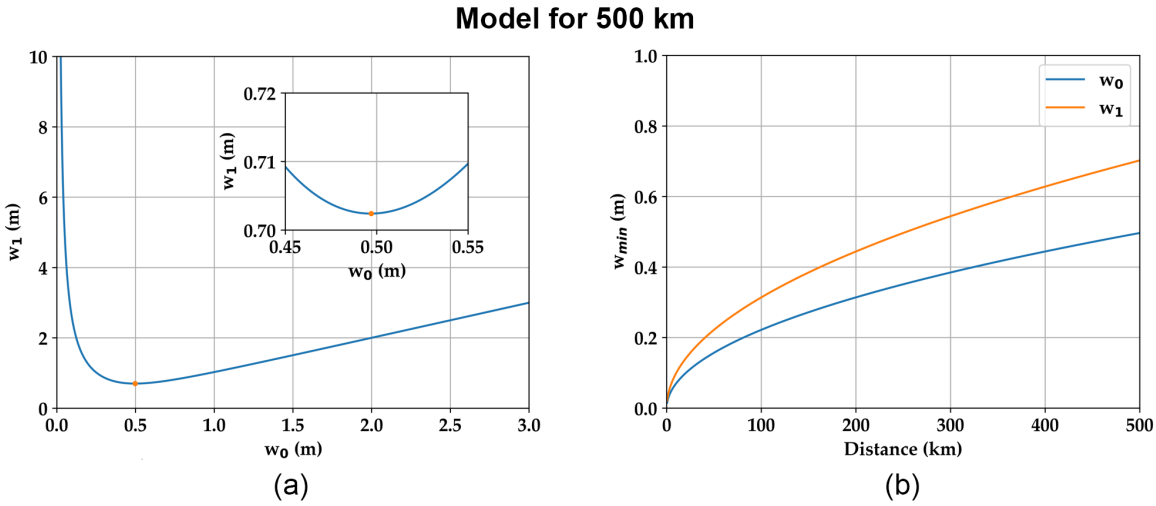



FIGURE 4.3: Model for 500 $km$: (a) minimization of $w_1$, (b) $w_{min}$ function of the distance.

Considering equation 4.5 for $z = 1\ km$, figure 4.2 and the size of a 1U CubeSat ($10cm \times 10cm \times 10cm$), one can analyse the transverse section of the beam as function of the propagated distance in a scaled model, presented in figure 4.4. The blue lines were drawn considering the minimizer waist placed at $z = 0$. One can see that at $z = 1\ km$, the beam covers the 2D array of thermoelectric generators. In this case, we get a spot size in the plasmonic photothermoelectric system that allows high energy transfer efficiency.

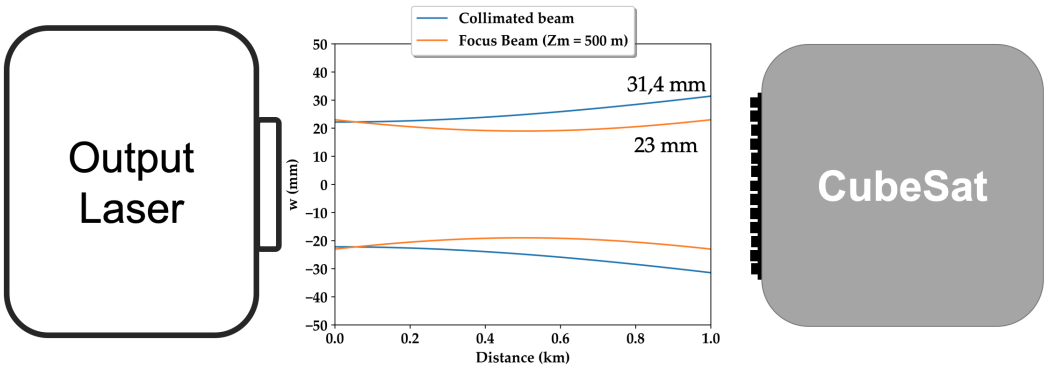



FIGURE 4.4: Model for 1 $km$ with scaled cross-sectional dimensions, of CubeSat and laser beam.

Because the final prototype of the WiPTherm project is for 1 $km$, we took a closer look at the propagation for that parameter. In figure 4.5 one can see different waist possibilities,

considering the 1 $km$ propagation. In this case, and depending on what CubeSat module we will deal with, we can always choose the desired final waist between the limits of figure 4.2.

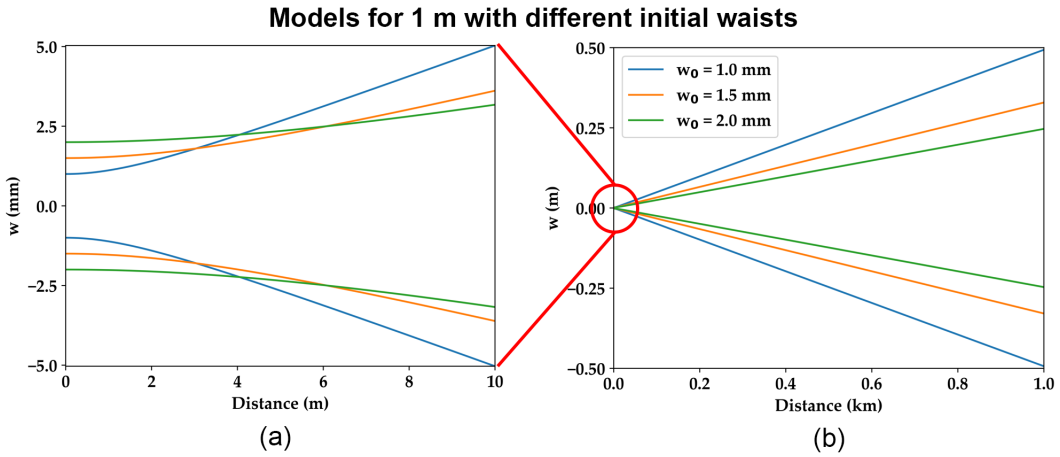



FIGURE 4.5: Visualization of waist over 1 $km$ for different values of $\omega_0$: (a) zoom of a region from main plot, (b) main plot.

To sum up this study of equation 4.5, table 4.1 appears.

| z | $w_0$ | $w_1$ |
|---|---|---|
| 1 $m$ | 0.99 $mm$ | 1.40 $mm$ |
| 1 $km$ | 22.21 $mm$ | 31.41 $mm$ |
| 500 $km$ | 0.496 $m$ | 0.702 $m$ |

TABLE 4.1: Minimum waist $w_1$ and minimizing waist $w_0$ for a propagation distance of $z = 1\ m$, 1 $km$, and 500 $km$.

500 $km$ is the typical orbit for Cubesats, and these results show us that the minimum waist that we can achieve is 0.702 $m$.

## 4.2 Analysis of light propagation under turbulent atmospheric conditions

In this section, it is presented the method used to propagate a 2D beam profile from one plane to another: the angular spectrum method. It is also discussed how to model turbulence, and in particular, results are presented for distinct propagation distances with the Von Karman turbulence phase screen.

### 4.2.1 Angular Spectrum Method

The goal was to have a numerical algorithm capable of evaluating a 2D beam profile at a given distance $z = z_0$, knowing its 2D profile at $z = 0$. For this purpose, we used the Angular Spectrum Method.

The first part of the method consists in decomposing a plane source $U(x, y, 0)$ into a summation of 2D plane waves $e^{2\pi i(f_x x + f_y y)}$ characterized by the spatial frequencies $f_x$ and $f_y$. That summation is exactly the integral:

$$U(x, y, 0) = \iint \widehat{U}_0\left(f_x, f_y\right) e^{2\pi i\left(f_x x + f_y y\right)} df_x df_y \tag{4.6}$$

where $\widehat{U}_0$ is the weight corresponding to the 2D plane wave $e^{2\pi i(f_x x + f_y y)}$.

$\widehat{U}_0\left(f_x, f_y\right)$ is called the "Angular Spectrum" [87] of $U(x, y, 0)$ and can be found by calculating the Fourier Transform of $U(x, y, 0)$:

$$\widehat{U}_0\left(f_x, f_y\right) = \frac{1}{2\pi} \iint U(x, y, 0) e^{-2\pi i\left(f_x x + f_y y\right)} dx dy \tag{4.7}$$

The second part of the method propagates each plane wave to the $z = z_0$ plane, separately. To do so, we can compare $e^{2\pi i(f_x x + f_y y)}$ to a 3D plane wave:

$$e^{i\vec{k}\cdot\vec{r}} = e^{(k_x x + k_y y + k_z z)} \tag{4.8}$$

where $\left\|\vec{k}\right\| = k = \sqrt{k_x^2 + k_y^2 + k_z^2} = \frac{2\pi}{\lambda}$. The formulation $e^{2\pi i(f_x x + f_y y)}$ describes $e^{i\vec{k}\cdot\vec{r}}$ in the $z = z_0$ plane, so $k_{x,y} = 2\pi f_{x,y}$ , and

$$k_z = \pm\sqrt{\left(\frac{2\pi}{\lambda}\right)^2 - k_x^2 - k_y^2} \tag{4.9}$$

The last step is to add all the propagated planes waves to find $U(x, y, z = z_0)$. Taking into consideration equations 4.6, 4.7 and 4.9 one can write the equation 4.10.

$$U\left(x, y, z_0\right) = \iint \widehat{U}_0\left(f_x, f_y\right) e^{2\pi i\left(f_x x + f_y y + z_0\sqrt{\left(\frac{1}{\lambda}\right)^2 - f_x^2 - f_y^2}\right)} df_x df_y \tag{4.10}$$

Equation 4.10 can be interpreted: if we want to propagate a beam profile from one plane to another, we have to add an extra phase term, which is the component $k_z$ of vector $\vec{k}$. One can look at 4.10 from a different perspective, and note that the integrals are exactly Fourier Transforms. So we can rewrite the same equation as:

$$U\left(x,y,z_0\right) = \mathcal{F}^{-1}\left\{\mathcal{F}\{U(x,y,0)\}(f_x,f_y)e^{2\pi i z_0\sqrt{\frac{1}{\lambda}^2-f_x^2-f_y^2}}\right\}(x,y) \tag{4.11}$$

Consequently, the method is summarized in the following 3 steps:

1. Sample the plane $z = 0$ and take its 2D Fast Fourier Transform (FFT);
2. Multiply each point of the 2D-FFT by a propagation term;
3. Take the 2D Inverse Fast Fourier Transform (IFFT) of that plane.

### 4.2.2 Atmospheric Turbulence

One of the effects that causes issues when we want to propagate a Gaussian beam through the atmosphere is turbulence. The concept of turbulence consists of a variation of the spatial refractive index $n$ caused, mainly, by local fluctuations of pressure and temperature. These variations can cause amplitude and phase oscillations on the propagated beam profile, worsening its quality.



FIGURE 4.6: The Starry Night by Vincent van Gogh (1889 painting) [88].

It is interesting to think about how to study and relate environmental parameters to turbulence effects in a laser beam [89]. The study of turbulence is separated in three different regions: strong, intermediate and weak. The regions of intermediate and strong turbulence are less studied than the weak ones. The study of these particular regions is very important and useful for the development of optical technology such as laser communication, imaging systems, remote detection and sensing, and, in our case, energy transfer. In an inspirational tone, one can analyse one of the famous Vicent Van Gogh's paintings in figure 4.6, The Starry Night, where the swirls represent wind and turbulence, Van Gogh's understanding of the cosmos as a living dynamic place [90].

Research groups modelled turbulence with spectral methods and random phase screens [91–94]. There are several models to emulate turbulence, such as the Tatarski [95], Kolmogorov [96], Von Karman [97], and Modified Von Karman Spectra (MVKS) [98]. One can compare these different models used to emulate turbulence in figure 4.7, where is plotted the power spectral density (PSD) of the refractive index of the medium divided by the structure parameter of the medium $C_n^2$ vs the spatial frequency.

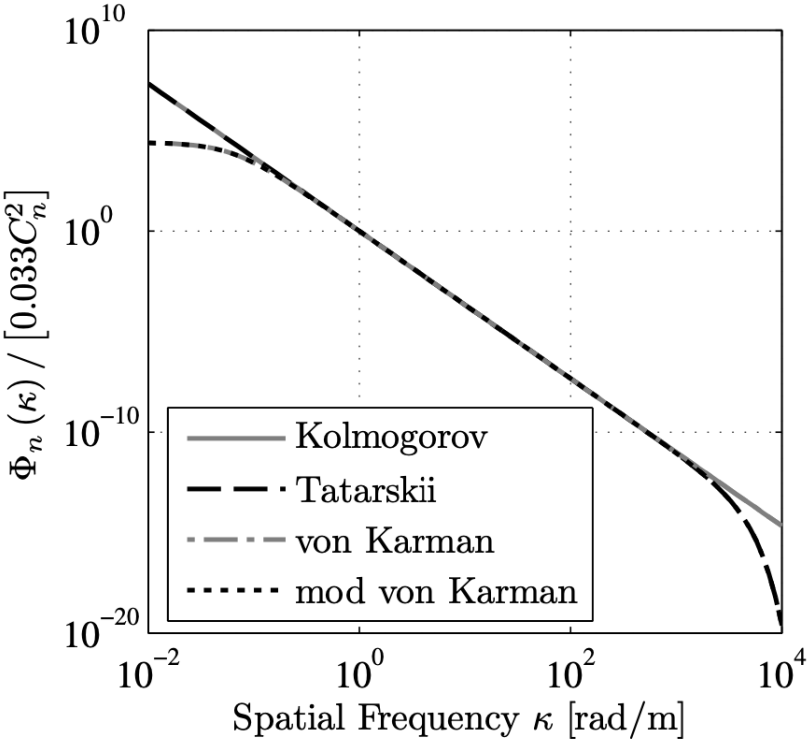



FIGURE 4.7: Common models for atmospheric power spectra [99].

An example of a turbulence model is the modified Von Karman spectrum. Its form is given by [98]:

$$\Phi_n(k) = 0.033C_n^2 \frac{\exp\left(-\frac{k^2}{k_m^2}\right)}{\left(k^2 + k_o^2\right)^{\frac{11}{6}}}, 0 \leq k \ll \infty \tag{4.12}$$

where the structure parameter of the medium is $C_n^2$ , $k_m = 5.92/l_o$ is an equivalent wavenumber related to the inner scale and represents the characteristic dimension of the smallest turbulent eddies, $k_o = 2\pi/L_o$ is the wavenumber related to the outer scale and it expresses the characteristic dimension of the largest turbulent eddies, and $k$ is wavenumber for the propagation inside the medium without any turbulence. Note that in equation 4.12, $\Phi_n(k)$ is called the PSD. If we consider the term $\exp(-\frac{k^2}{k_m^2})$ always equal to 1, we get the original Von Karman PSD model.

The outer scale parameter $L_0$, near the ground, is approximately $h/2$ , where $h$ is the height above ground. Typical numbers quoted for $L_0$ vary between 1 and $100m$, depending on atmospheric conditions and the geometry of the specific experiment [100]. For $K$ larger than some critical wavenumber $k_o$, the shape of PSD is determined by the physical laws that govern the breakup of large turbulent eddies into smaller ones. Then, PSD can be predicted from physical laws governing turbulent flow [101].

As previously specified, phase screens aim to simulate random phase perturbations resulting from random index fluctuations in extended atmospheric turbulence and, in literature, one can find the numerical ranges for the structure parameter $C_n^2$ defining strong, intermediate and weak turbulence [102]:

$$\begin{aligned} &C_n^2 > 10^{-14}\ \mathrm{m}^{-2/3} && \text{strong} \\ &10^{-16} < C_n^2 < 10^{-14}\ \mathrm{m}^{-2/3} && \text{intermediate} \\ &C_n^2 < 10^{-17}\ \mathrm{m}^{-2/3} && \text{weak} \end{aligned} \tag{4.13}$$

The above-presented values of the structure parameter are necessary to define the turbulence regime. It should be noted that the parameter $C_n^2$ varies as a function of altitude, location, and time of day. This parameter has been studied over the years and it was extensively measured as a function of altitude above the earth [103–116]. This parameter is the structure constant of the refractive index fluctuations and it serves as a measure of the strength of these fluctuations. Several models were achieved with data measurements, however, they have a strong dependence on the geographical location and other conditions such as weather conditions and seasons of the year.

The SLC-Day model tries to segment the atmosphere into layers with different $C_n^2$, considering equation 4.13, and it is given by [117]:

$$C_n^2(h) = \begin{cases} 0 & 0\text{ m} \leq h < 19\text{ m} \\ 4.008 \times 10^{-13} h^{-1.054} & 19\text{ m} \leq h < 230\text{ m} \\ 1.300 \times 10^{-15} & 230\text{ m} \leq h < 850\text{ m} \\ 6.352 \times 10^{-7} h^{-2.966} & 850\text{ m} \leq h < 7000\text{ m} \\ 6.209 \times 10^{-16} h^{-0.6229} & 7000\text{ m} \leq h < 20,000\text{ m} \end{cases} \tag{4.14}$$

so $C_n^2$ is now function of the altitude $h$. This model agrees with experimental data from atmospherical ascending balloons [118].

Regarding this $C_n^2$ parameter, one can relate it with the so-called Fried parameter $r_0$ :

$$r_0 = 0.185 \left[ \frac{4\pi^2}{k^2 L c_n^2} \right]^{3/5} \tag{4.15}$$

where $k$ is the unbounded wave number, and $L$ is the propagation distance. The Fried parameter characterizes the phase fluctuations of the specific phase screen utilized to model the random phase distribution. It also describes the transverse coherence length, the inner and outer scales that control the total aberration perceived by the propagating beam.

For the generation of a random phase screen, we used AOtools [119], an open-source Python package focused on providing tools for adaptive optics users and researchers. It contains "tools for adaptive optics processing, including analyzing data in the pupil plane, images and point spread functions in the focal plane, wavefront sensors, modelling of atmospheric turbulence, physical optical propagation of wavefronts, and conversion between frequently used adaptive optics and astronomical units" [119].

AOtools utilizes an interesting method for simulating infinitely long and nonstationary phase screens with optimized memory storage [120]. AOtools also provides functionalities to create finite Kolmogorov and Von Karman turbulence phase screens. We decided to use this package to generate our phase screens.

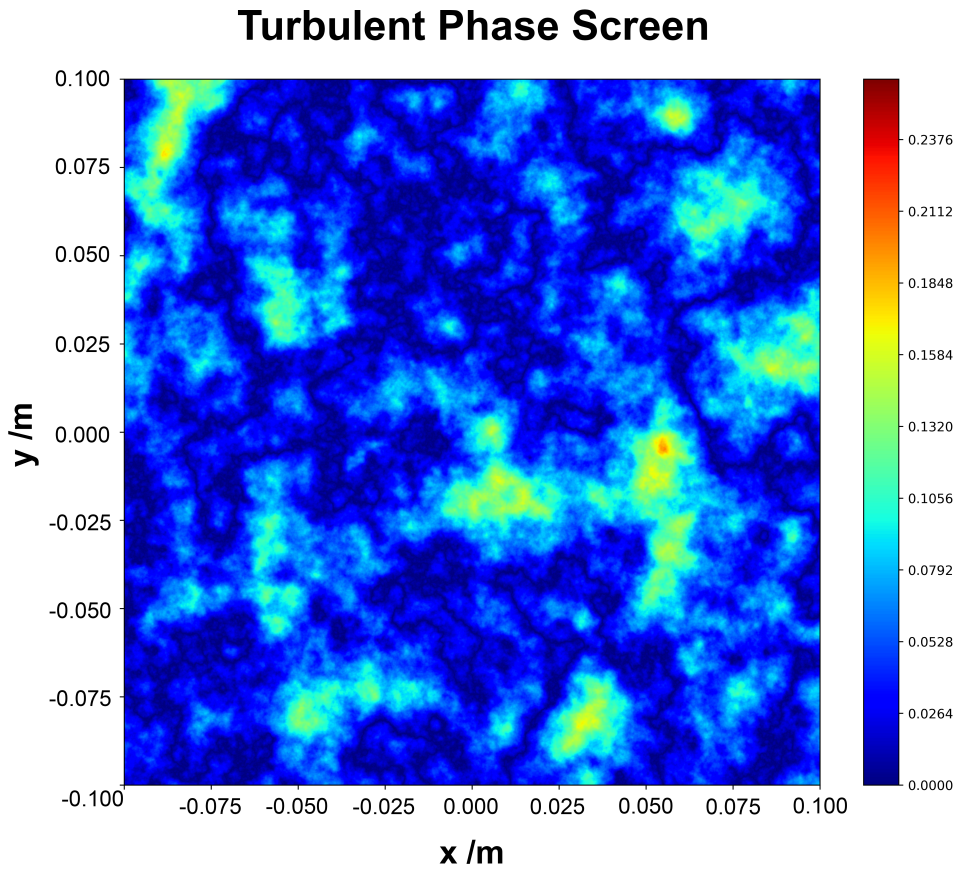



FIGURE 4.8: Example of a phase screen generated with a function from AOtools.

The library also includes methods to create infinite Kolmogorov and Von Karman phase screens using the methods described by Assémat and Wilson [120]. One can see in figure 4.8 an example of the generation of an infinite phase screen [120, 121] using the "infinitephasescreen.PhaseScreenVonKarman" AOtools' function. The scale represents the absolute value of the phase.

### 4.2.3 Simulation's algorithm

In figure 4.9, a flow chart will describe how the developed code runs the method. The code starts by defining the initial conditions. First, we create a Gaussian beam profile with a waist $w_0$ in a grid with $N \times N$ pixels. This $N$ parameter must be a power of 2 because it allows us to perform the 2D FFT scaling with $O(N \times log(N))$, instead of $O(N^2)$. This is a great improvement when we talk about speed: considering an initial plane $N \times N$ with $N = 2^{13}$, it takes much less running time (almost half) than the $N = 2^{13} - 1$. After creating the Gaussian beam profile, one needs to choose the dimensions of the problem, such as

the wavelength (in our case 1550 $nm$), the number of phase screens, the spacing between them, and also the propagation size. Then, we evaluate the intensity integral to compare it to the final one. Therefore, we use the Angular Spectrum method, which starts by calculating the spatial frequencies $f_x$ and $f_y$ and the FFT of the input complex amplitude profile. If we are dealing with a problem with turbulence, the algorithm generates a Von Karman Phase Screen with AOTools and multiplies it by the initial spectrum; if we are dealing with a problem where turbulence is insignificant, one can skip the previous step and multiply directly the initial spectrum by the free propagation term. If we want to pass the beam through another PS and propagate it again we can generate another random PS and multiply by another free propagation (FP) term, as many times as we like, and even with different Phase Screens and different propagation distances. Following all those steps, the IFFT is then calculated to get the final beam profile. At this point, the analysis stage appears and one can study the final beam profile and compare it to the initial one.

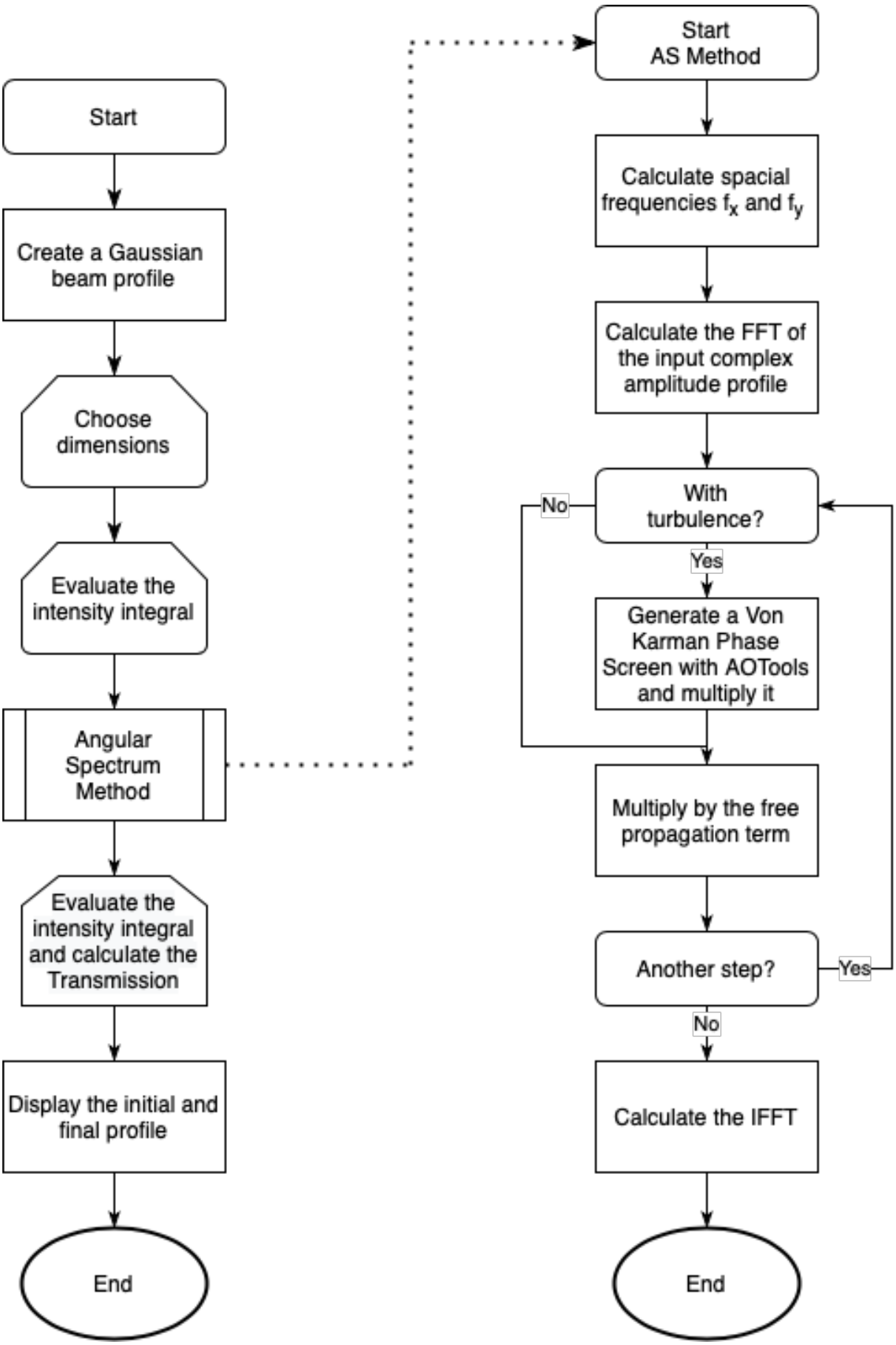



FIGURE 4.9: Flow chart of the developed code.

A scheme of the code can be seen in figure 4.10. The original beam is converted into its 2D FFT and then it can propagate freely until the first random PS, then again do its free propagation and find a second PS, and it can do this as many times as we want. In the end, we take the 2D IFFT to get the final beam profile. The phase screens in figure 4.10 were generated using the Von Karman Spectra (VKS) with AOTools.

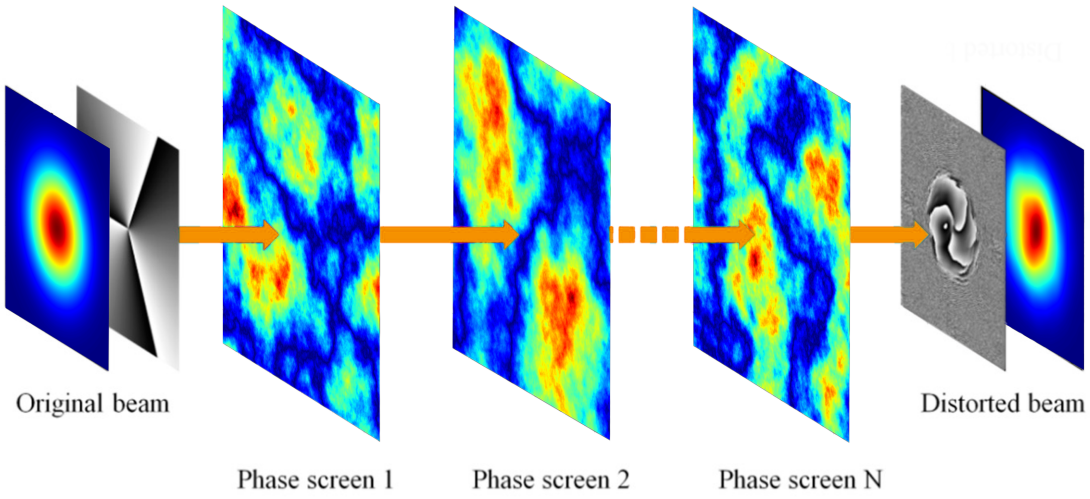



FIGURE 4.10: Turbulent atmospheric propagation simulation scheme.

## 4.3 Simulation results

### 4.3.1 Preliminary results

To test the algorithm, some initial tests were done. In the first one, we had the objective of confirming the free propagation of the Gaussian Beam. So we created a 2D Gaussian profile simply by calculating:

$$Gaussian\ profile = \frac{1}{2\pi\sigma^2} \times e^{\frac{-x^2+y^2}{2\sigma^2}} \tag{4.16}$$

with $\sigma = 0.005\ m$. The generated profile can be seen in figure 4.11.

The beam profile from figure 4.11 was propagated with the Angular Spectrum Method through 1 $km$, considering $\lambda = 1550\ nm$. The result is shown in figure 4.12. One can see that the beam has expanded.

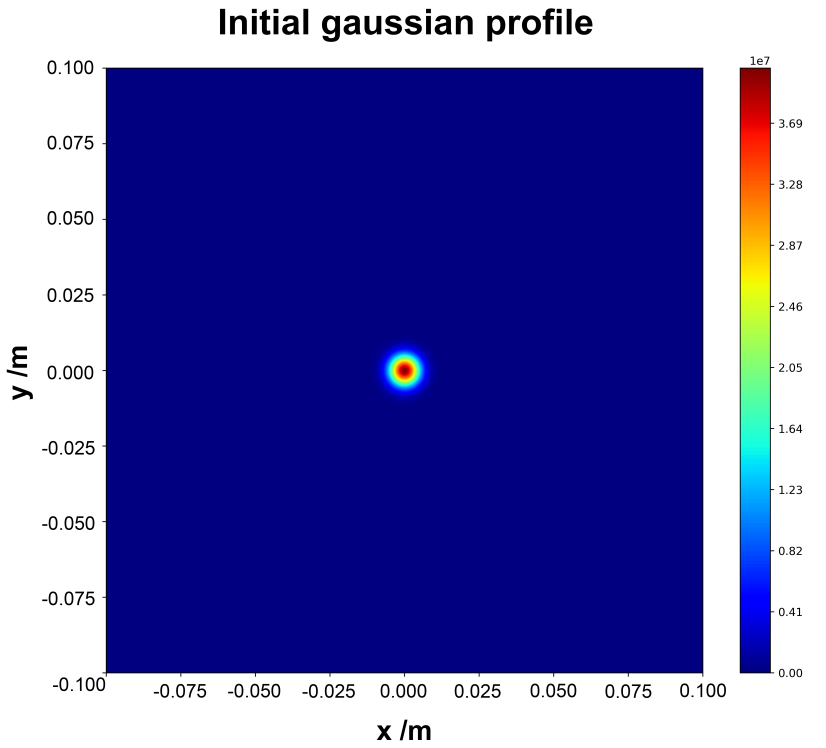



FIGURE 4.11: Initial Gaussian beam.

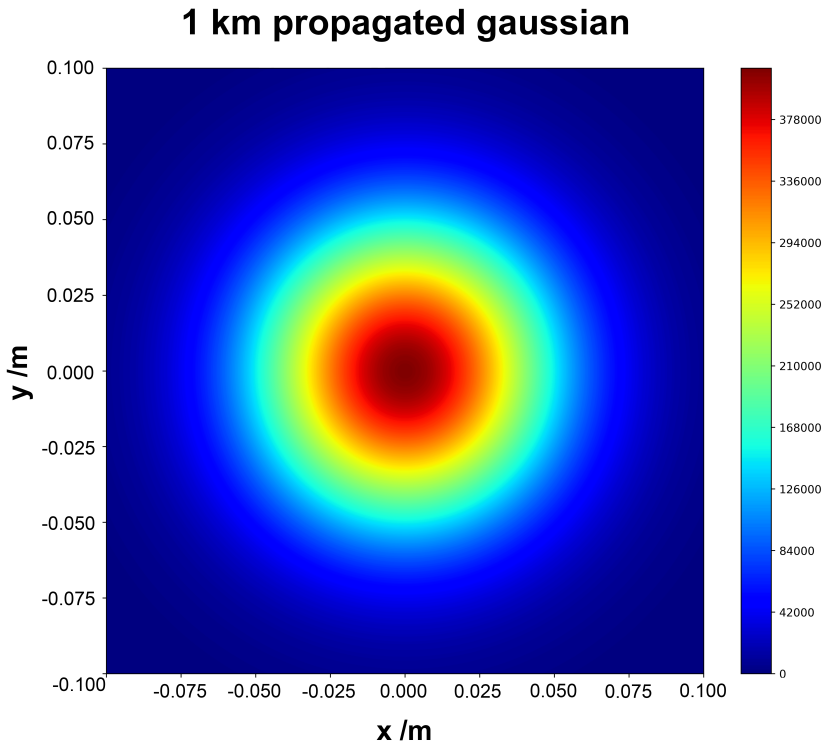



FIGURE 4.12: 1 *km* free propagation of the initial Gaussian beam.

If we take into consideration equation 4.5, and evaluating the beam waist in the numerical 2D grid (a bisection method over the $x$ axis to find $1/e^2$ intensity point), we get an error of 0.34%. This happens because of the discretization of the source plane (grid). Nevertheless, the results are good enough to say that the algorithm is running as it should and we can therefore start to add some turbulence.

After checking the angular spectrum method, we wanted to test the propagation of the initial Gaussian beam through 1 $km$ and through a Von Karman PS placed in the middle of the propagation distance (500$m$). The result, for a Von Karman PS generated with the parameters $r_0 = 18.99\ m$, $L_0 = 8\ m$, and the size of each pixel upscaled by a factor of 30, is shown in figure 4.13. One can see that the shape of the beam is changed.

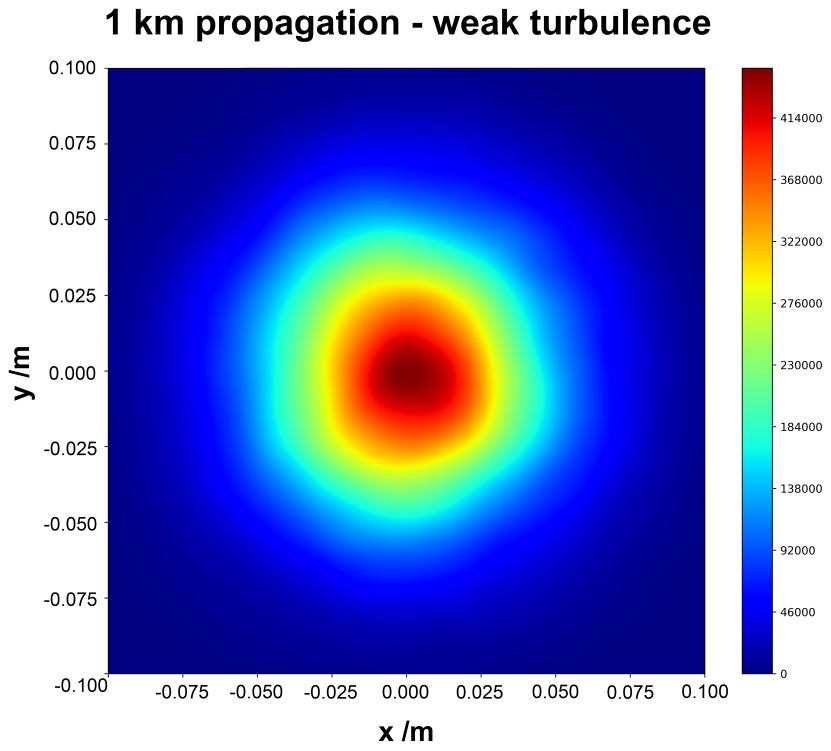



FIGURE 4.13: 1 $km$ propagation of the initial Gaussian beam with turbulence, $r_0 = 18.99\ m$

To have a comparison term, we did the same simulation but only changed the $r_0$ value to $r_0 = 1\ m$. Figure 4.14 shows this result, and the expected extra turbulence caused the seen effect. The Gaussian beam is distorted and the spot has now a different shape. The maximum intensity point is shifted $\approx 3\ cm$.

These results show us that, with the algorithm and with intense PS, the beam can be distorted and achieve some peculiar profiles under turbulent propagation conditions.

In the next subsection, we show the study of the beam turbulent propagation using the SLC-Day model [117] that tries to segment the atmosphere into layers with different $C_n^2$, considering equation 4.14.

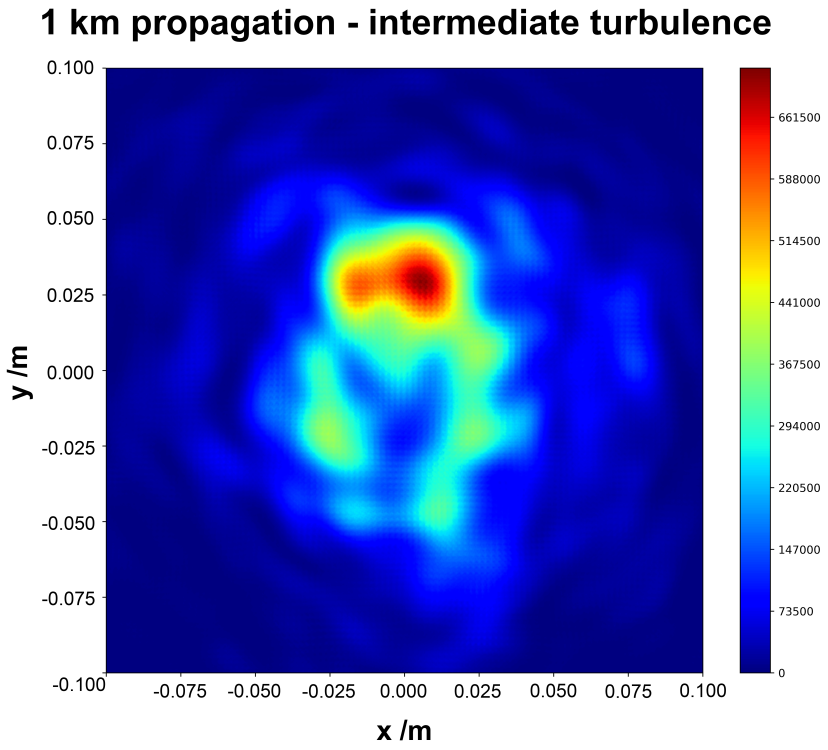



FIGURE 4.14: $1km$ turbulent propagation of the initial Gaussian beam with turbulence, $r_0 = 1\ m$

### 4.3.2 Results using the atmospheric layer model

In this subsection we will present some results using the atmospheric layer model to control the $C_n^2$ parameter. This model is presented in the equation 4.14.

To study the propagation of a 1550 $nm$ Gaussian beam of light through 7 $km$ of atmosphere we considered the scheme in figure 4.15. We start with a free propagation of 19 $m$. Then the beam passes through a random PS* placed at $19^+$ $m$, generated with the VKS and the $C_n^2(h)$ parameter was calculated in the middle of the distance between the first PS and the second one at $h = \frac{19+230}{2}$ $m$. After that, the beam freely propagates to the mark of 230 $m$. There, it is affected by the random PS placed at $230^+$ $m$, again, generated with the VKS with the parameter $C_n^2(h)$ calculated in the middle of the distance between the

*all the generated phase screens were calculated using the AOTools function "turbulence.phasescreen.ft_phase_screen", and the source code is present in Appendix A

second PS and the third PS ($h = \frac{230+850}{2}\ m$). The beam propagates in free space to 850 $m$ where it finds another random PS, generated with a $C_n^2(h)$ parameter evaluated in the middle of the distance between the third PS and the fourth one, at $h = \frac{850+2000}{2}\ m$. The final phase screen is placed at $2000^+\ m$, and it was generated with a $C_n^2(h)$ calculated at $h = \frac{2000+7000}{2}\ m$. So the beam propagates until there, suffers the turbulence effect, and then propagates again in free space to the 7000 $m$ final mark.

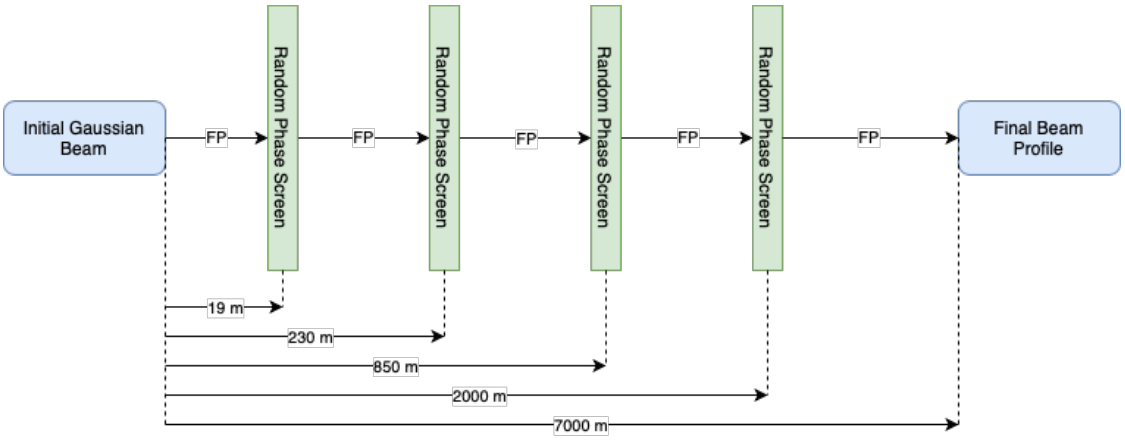



FIGURE 4.15: Simulation scheme for 7000 $m$ propagation

We simulated exactly the propagation as described above. We took snapshots just before each PS: before 19 $m$, 230 $m$, 850 $m$ and 2000 $m$, and finally we took the final image at $h = 7000\ m$. The result for 19 $m$ propagation is in figure 4.16. Here one can see that the beam keeps its Gaussian shape.

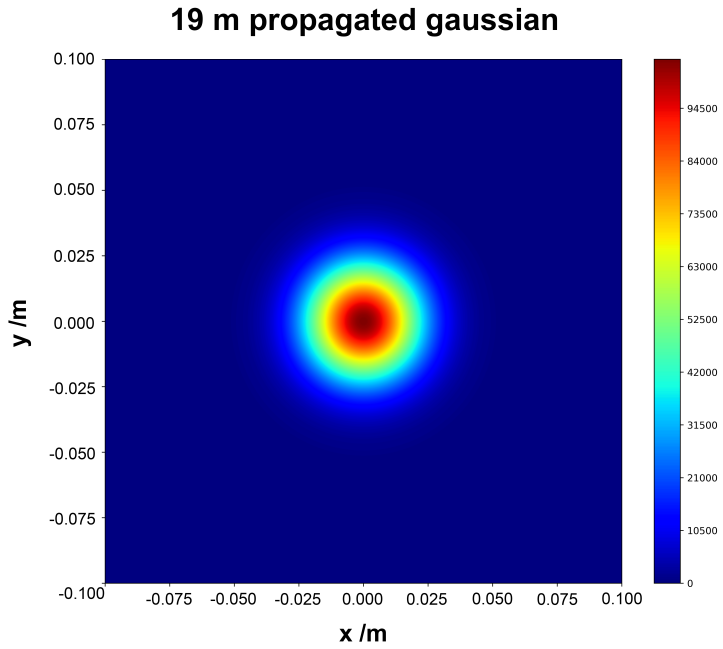



FIGURE 4.16: Beam profile after 19 $m$ of free propagation.

After that, the beam finds the PS of figure 4.17.

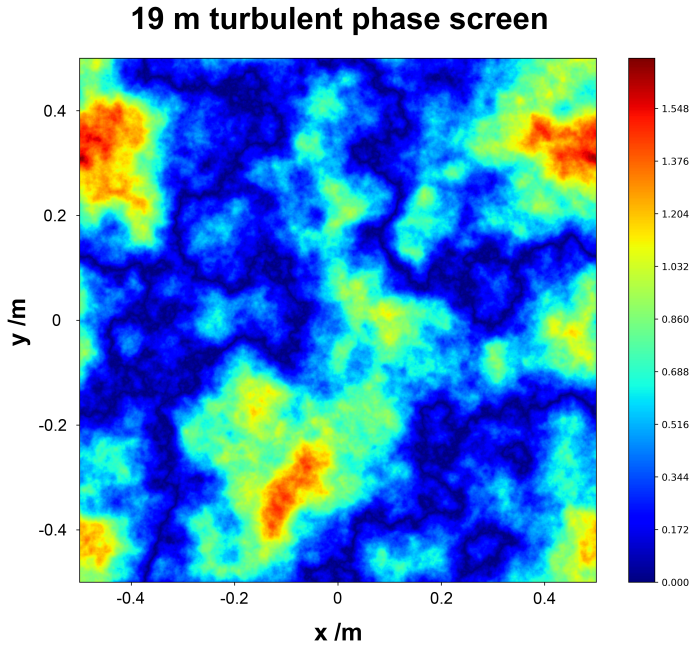



FIGURE 4.17: Turbulent Phase Screen placed at $19^{+}$ $m$.

Then, the beam propagates until 230 $m$ and the result is shown in figure 4.18. One can see that the beam has now an irregular shape and not a perfectly Gaussian one.

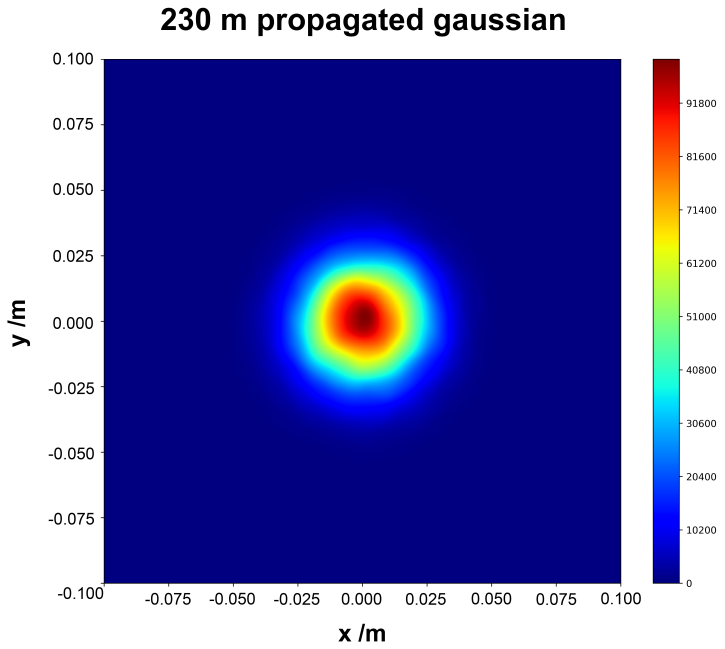



FIGURE 4.18: Beam profile after 230 $m$.

Once again, the beam reaches a turbulent PS placed at $h = 230\ m$ that can be inspected in figure 4.19.

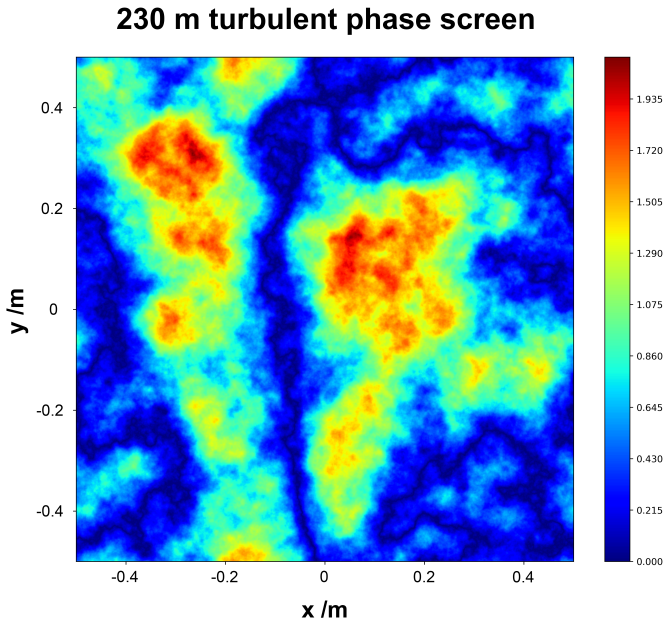



FIGURE 4.19: Turbulent Phase Screen placed at $230^{+}\ m$.

Now, it is time to analyse the result for $h = 850\ m$ in figure 4.20. We start to notice a small deviation of the beam to the center (going to positive values of $x$ and $y$). The shape

is more irregular, and of course, we can notice the beam expansion.

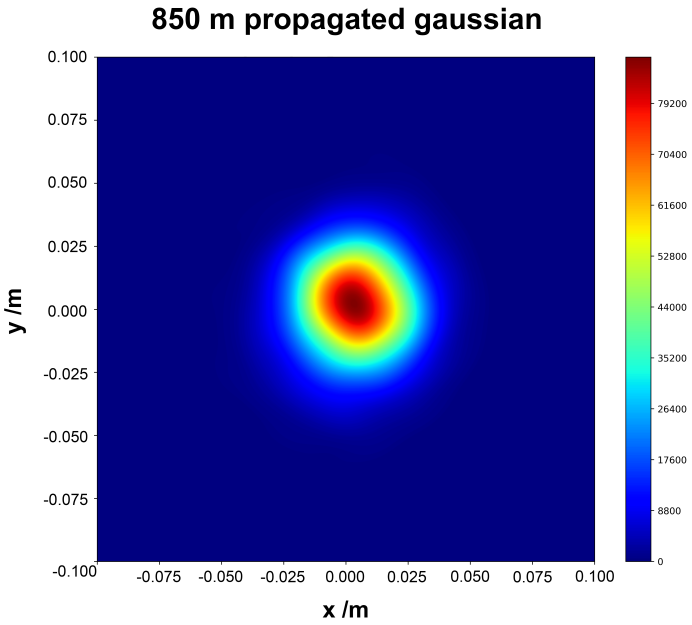



FIGURE 4.20: Beam profile after 850 $m$.

At $h = 850\ m$, the beam interacts with the PS that can be checked in figure 4.21.

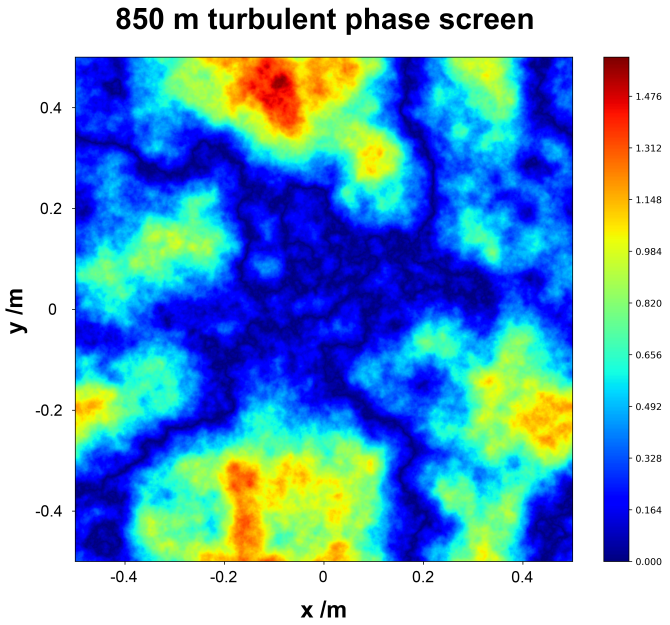



FIGURE 4.21: Turbulent Phase Screen placed at $850^{+}\ m$.

The result of the propagation through 2000 $m$ is visible in figure 4.22. This figure reaffirms and emphasises the conclusions taken in figure 4.20.

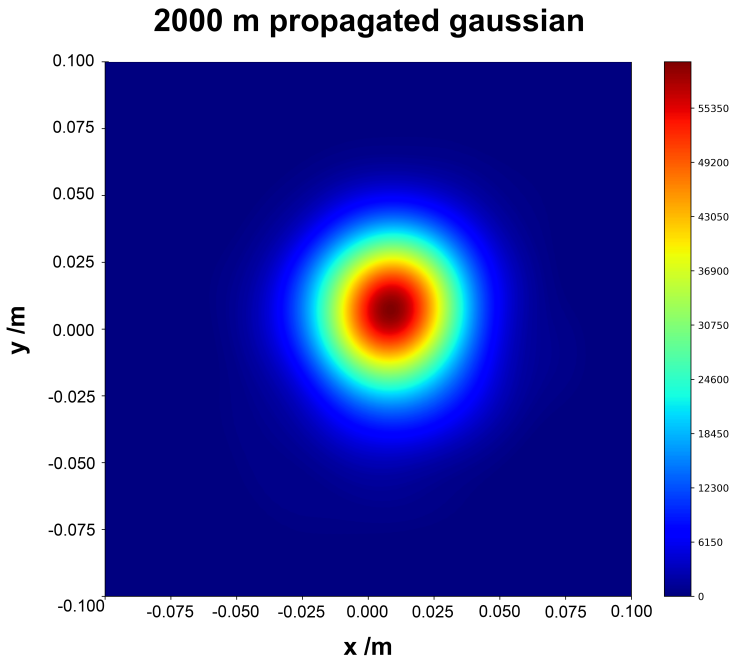



FIGURE 4.22: Beam profile after 2000 $m$.

Once again, the beam passes through a random PS located at $2000^{+}$ $m$ (figure 4.23).

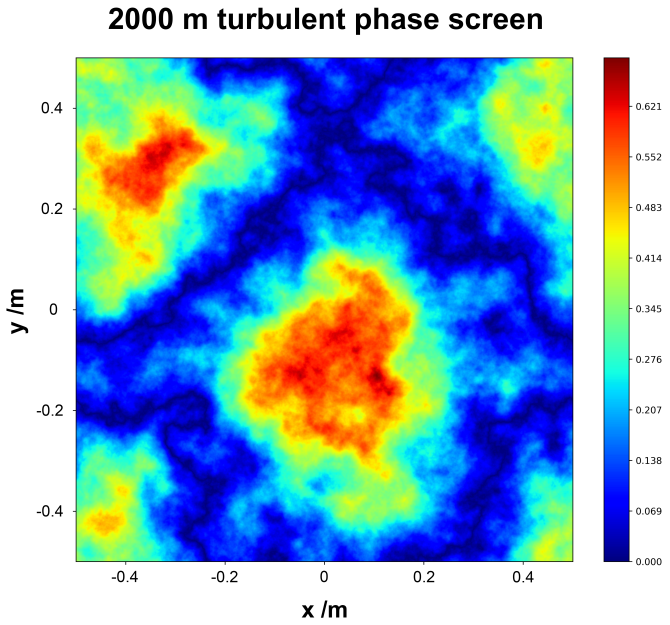



FIGURE 4.23: Turbulent Phase Screen placed at $2000^{+}$ $m$.

Finally, the beam propagates until it reaches 7000 $m$ and now we are in the condition of plotting the final beam profile on figure 4.24. The $x$ and $y$ axes scales were not changed

because we were interested to investigate the center deviation of the beam. In this case, the beam has a deviation of $\approx 3.5\ cm$.

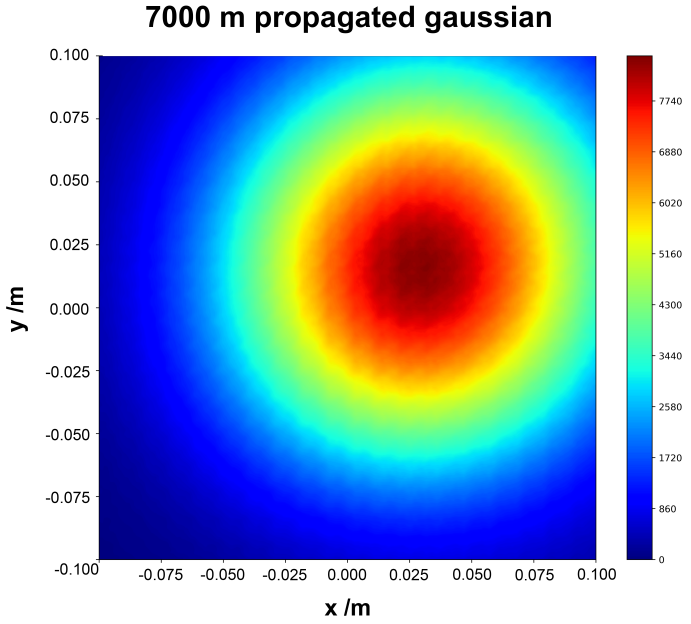



FIGURE 4.24: Beam profile after 7000 $m$.

At this moment, we were interested to analyse the beam propagation through 7000 $m$, but this time considering different phase screens (turbulence). We repeated the simulation from the beginning, but we changed all the random seeds used for the phase screens generation. The result for the second simulation can be seen in figure 4.25. One can notice that the beam suffered a deflection of $\approx 5.3\ cm$ in a different direction.

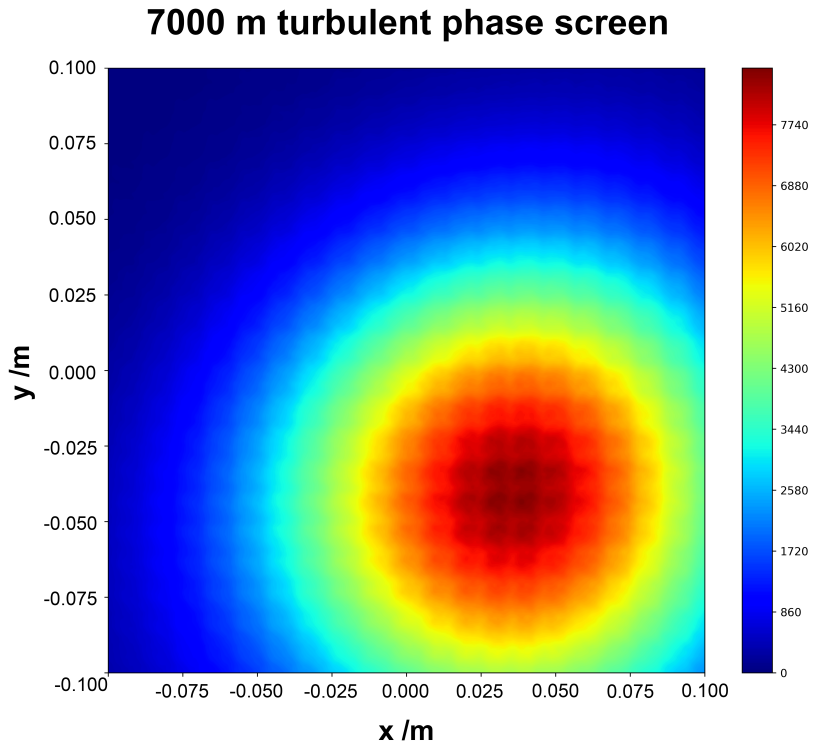



FIGURE 4.25: Beam profile after 7000 $m$ with different random PS.

To get a better understanding of the beam deviation, we did 1000 simulations just like these, where we changed all the random PS seeds, and consequently, all the simulations have different conditions. The centers' representation of all 1000 simulations are shown in figure 4.26. The right colour bar shows the relative deviation to the center. One can see that the concentration is very high near the center and it starts to fade as we move away from it.

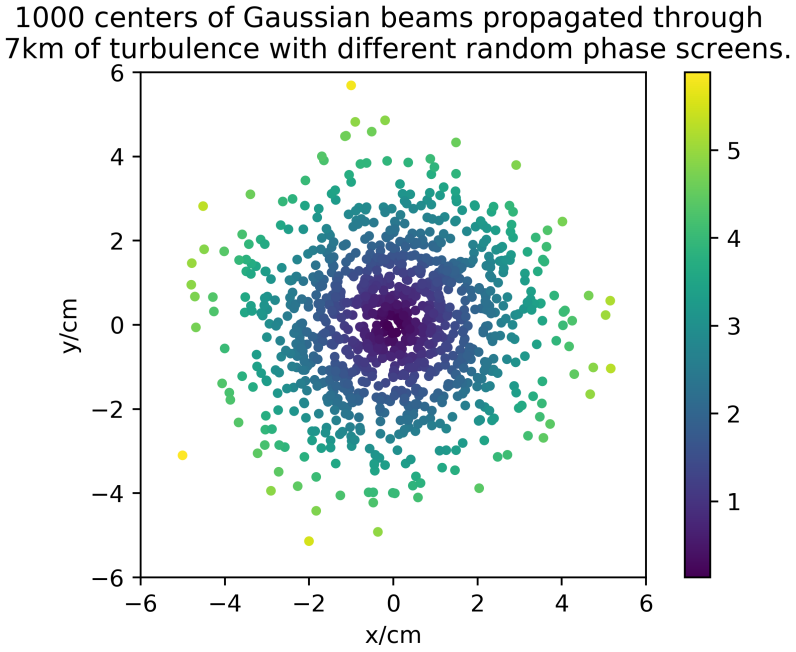



FIGURE 4.26: 1000 different centers of Gaussian beams after propagating 7 *km* of turbulent atmosphere.

The translation of the above figure is the histogram present in figure 4.27. One can see the distribution of the beam deviation relative to the center after the original Gaussian beams propagates 7000 *m*. Observing the histogram, we can say that the beam is not likely to deviate more than 6 *cm*.

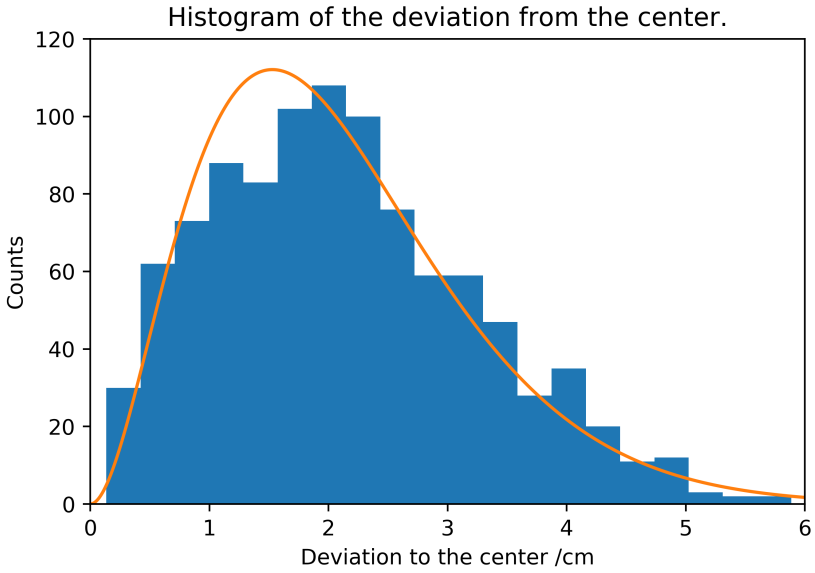



FIGURE 4.27: Histogram of the center of the beam deviation after 7 *km* of turbulent atmosphere with respective fit.

Analysing the histogram of figure 4.27, it seems like the distribution does not follow a normal behaviour. Because of this fact, we tried to fit our data with the following expression:

$$F(x) = A \cdot x^2 \cdot \sqrt{\frac{2}{\pi}}/w \cdot \exp\left(-2 \cdot ((x - xc)/w)^2\right) \tag{4.17}$$

using the scaled Levenberg-Marquardt algorithm with a tolerance of 0.0001, obtaining a $R^2 = 0.93$. The orange curve in figure 4.27 represents this fit, and one can see that it is trying really hard to fit the data. It would be possible, looking at equation 4.17, to refine/add some parameters to force the fit, but we choose this function keeping in mind the problem of over-fitting.

Figure 4.27 also tells us that the probability of the beam being deflected 2 $cm$ is very high. Hence, we were curious about the mean and standard deviation of this variable and in table 4.2 we can see the results for both values. The mean value is $\bar{x} \approx 2.369$ $cm$ and the standard deviation is $\sigma \approx 1.298$ $cm$.

| Parameter | Value(cm) |
|---|---|
| Mean $(\bar{x})$ | 2.369 $cm$ |
| Standard Deviation $(\sigma)$ | 1.298 $cm$ |

TABLE 4.2: Mean and standard deviation of 1000 samples of the beam deflection after propagating 7 $km$ in turbulent atmosphere.

## 4.4 Final remarks and future work

The numerical results for the beam expansion tell us that it is possible to achieve a minimum waist of 0.702 $m$ after a propagation of a regular 500 $km$ CubeSat orbit. Since 3U CubeSats have foldable thermometric panels with total dimensions of $40 \times 30$ $cm$, with a simple calculation one can perceive that only $\approx$ 8% of the beam area would be used in the transmission of energy to orbiting CubeSats. For the 1 $km$ test, a 1U CubeSat will be used with a thermo-electric panel with dimensions of $10 \times 10$ $cm$, and for this propagation distance, the beam profile perfectly matches the target.

The turbulence atmospheric propagation simulation showed us that for 7 $km$ propagation, altitude above the most turbulent region, the beam deflects on average $\approx$ 2.369 $cm$

with a standard deviation $\sigma \approx 1.298\, cm$. This is a very important result for aiming purposes. In a future work, it would be interesting to measure the temporal or spatial fluctuations in the irradiance of the beam profile caused by the phase screens; it would also be intriguing to demystify the dependence of the number of phase screens on the beam profile; it would be attractive to study turbulence using different prediction models for beam attenuation through the atmosphere.

# Chapter 5

# High-Power Fiber Laser

## 5.1 Experimental Setup

High average power and transverse single-mode propagation are two key parameters for the final objectives of the thesis. In the state of art, the main advantages of double-clad laser/fiber are mentioned. The double-clad step-index fiber design was selected due to the possibility of reaching high average power, thanks to the combination of the high numerical aperture of the inner cladding and the use of high-power pump laser diodes. The low numerical aperture of the fiber core permits maintaining a transverse single-mode propagation.

The composition of the two high-index silica-doped materials had to be carefully determined to integrate the fiber system: one doped with Erbium and Aluminium, corresponding to the future fiber core, and the other one only doped with Aluminium corresponding to the future fiber cladding. The maximum Erbium ion concentration seems to be ideal to maximize the pump absorption, minimizing the fiber length required to realize the laser source.

When active ions are too close in the host, they tend to form clusters allowing energy transfer between them, which can seriously degrade the gain and power efficiency by processes which are called quenching. To circumvent this issue, the group of the Université of Limoges used an Aluminium co-doping which has the property of helping the solubilization of rare-earth ions in the silica host, thus limiting the clustering effect. However, it is only possible to a certain extent because when the Aluminium concentration becomes too important, crystallization starts to occur. In addition, once the composition of the future fiber core has been chosen, it is necessary to find the adequate composition

for the future fiber cladding in order to obtain a single-mode propagation while keeping fiber flexibility, i.e. the possibility to use the fiber with a bending radius lower than 15 $cm$.

In figure 5.1, one can see the chosen fiber design, created by the Université of Limoges for the WipTherm project. This fiber design has an external coating made of high-index polymer to ensure mechanical stiffness. To ensures pump light guidance, high NA air-cladding (with $D = 160\,\mu m$) was incorporated, which has a better thermal resilience compared to low-index polymers and it also allows high pump power handling. The background cladding is characterized by high-index, and 8 fluorine-doped inclusions have been added to enhance pump absorption by virtually increasing the core-to-clad ratio and suppressing non absorbed whispering gallery cladding modes. Last but not least, the fiber has a 25 $\mu m$ Erbium-doped core. Large core diameters are twofold: first not only to enhance the signal but also to decrease fiber length through an increase in the cladding absorption for the pump light [45].

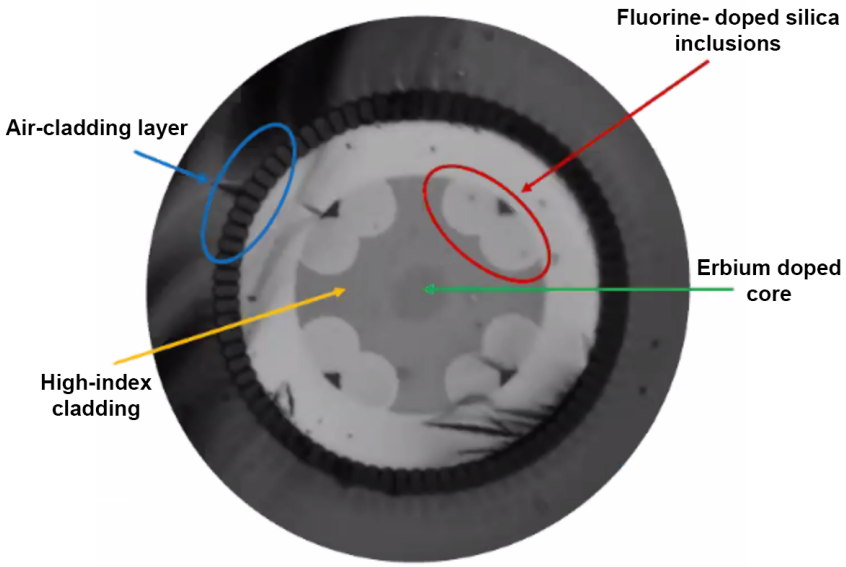



FIGURE 5.1: Sectional cut of the fiber.

At the University of Limoges, the optical refractive index profile (RIP) along the fiber's length was studied, with sub-micron spatial resolution, after producing the fiber. This was only possible due to the IFA-100 Interferometric Fiber Analyser, and the profile can be visualized in figure 5.2.

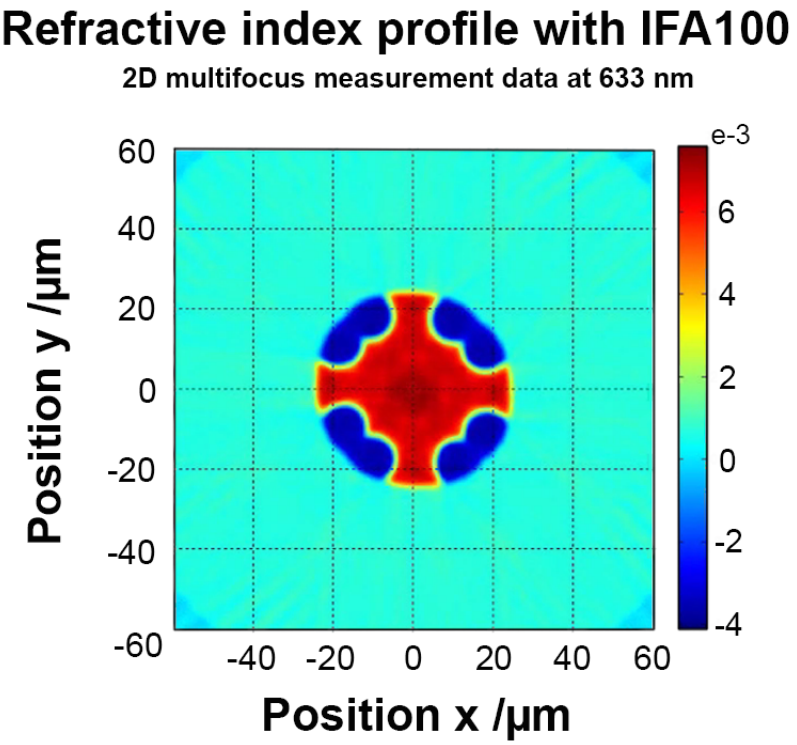



FIGURE 5.2: Refractive index profile of the developed fiber analysed at 633 *nm* with IFA-100. The right bar represents the differential values of the refractive index.

This type of profile is very particular and allow us to minimize the skew rays, maximizing the meridional rays and thus maximizes the pump absorption inside the core. The pump absorption is not only enhanced by this circular symmetry breaking but also due to the virtual increase of the core-to-clad ratio.

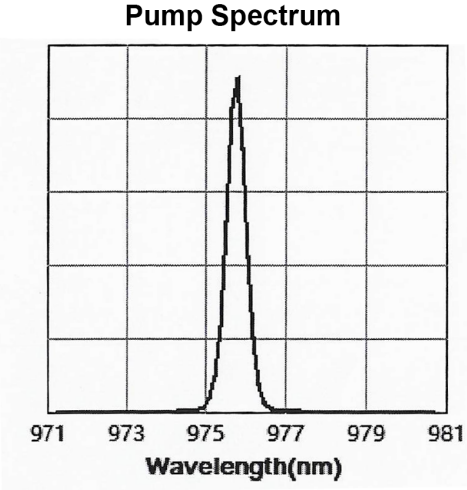



FIGURE 5.3: Laser pump spectrum provided by the manufacturer datasheet. Vertical axis will represent optical intensity.

For our laser setup, our pump laser is a wavelength-stabilized laser centered at 976 $nm$, with a maximum output power of 140 $W$; it is a high brightness fiber coupled diode laser from BWT [122]. The spectrum of this pump laser can be seen in figure 5.3 and the curve of power as a function of the supplied current in figure 5.4.

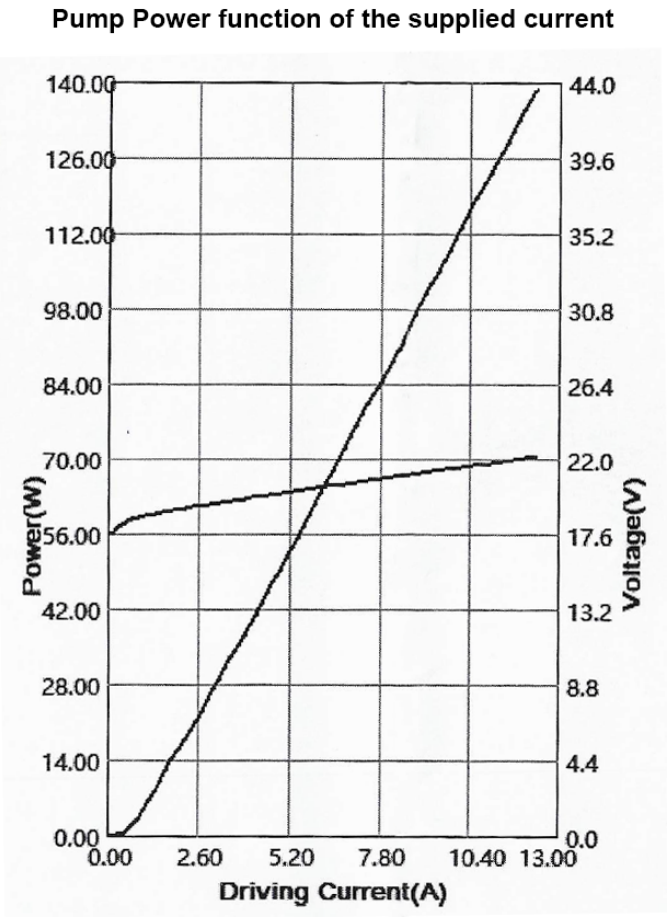



FIGURE 5.4: Pump power as a function of the supplied current, from the data sheet 5.4.

The conceived laser setup can be seen in figure 5.5. It is a setup similar to the one that Zhou et al. designed [123], but upgraded and applied to our work. Firstly, the pump laser light exits the fiber and expands. One can collimate it with the aspheric lens $L_1$ placed at its focal length from the fiber. The beam now propagates until it reaches $L_2$, the aspheric lens with an anti-reflective coating to the $1050 - 1620\ nm$ wavelengths, and it is injected into the fiber. Stimulated emission occurs and both the laser light and the residual pump light exit the fiber, expanding. The laser light is now collimated with the aspheric lens $L_3$ and it is reflected in the short pass dichroic mirror $M2$ (with reflectivity, from $1500nm$ to $1650nm$, higher than 99%), while the residual pump is transmitted in $M2$ (98.48% of transmission), falling into a beam trap. The laser light is now re-injected in the fiber and

follows the same path, but in the opposite direction (in figure 5.5, from right to left), reaching the dichroic mirror $M1$ where it will be reflected. The output can be measured with a power meter. It is possible to add a wedge to divide the beam and analyse it with a Short Wave Infra-Red (SWIR) camera.

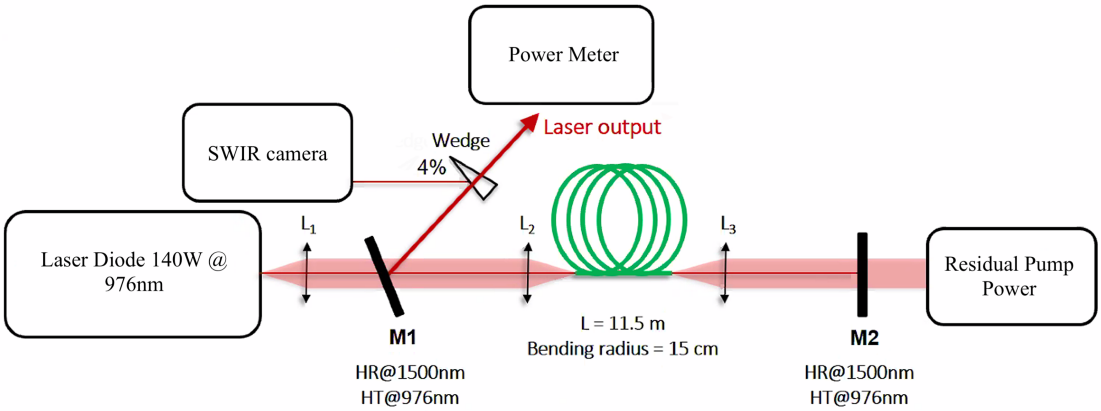



FIGURE 5.5: Experimental setup of the High Power Fiber Laser

Something to note is the fact that this laser has no resonant cavity, no photon at the output passes more than twice in the active medium, and so feedback does not exist. Although the output has some coherence, and narrow spectrum, it does not have the spectral selectivity normally associated with a laser.

## 5.2 Results and discussion

After a careful and precise alignment, we could take the astonishing picture of figure 5.6. One can see all the fiber illuminated with the characteristic green colour of erbium. One fun fact is that the camera also captured the near-infrared light, expressed in purple, which is invisible to the human eye.

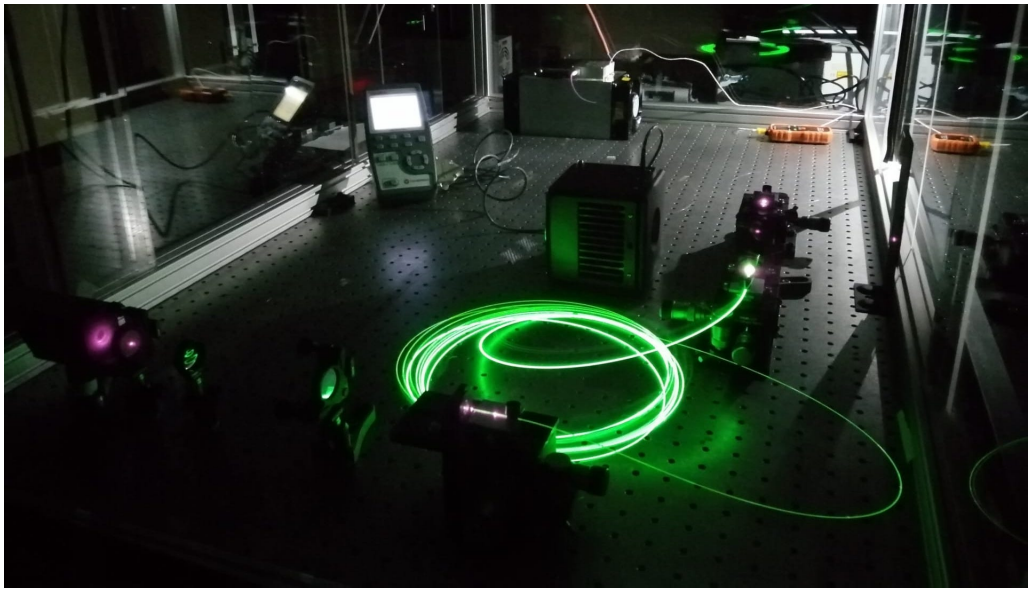


FIGURE 5.6: Picture from the real setup.

The output laser power was plotted as a function of the pump power in figure 5.7. We can clearly see a regular laser behaviour for relatively low power (pump power lower than 55 $W$): laser pump power is zero until the system has enough energy to have population inversion; after that, the number of the output photons (or laser power) must depend linearly on the pump power. When we reach high pump power ($> 70$ $W$), the experimental data starts to deflect from our trend line, thus limiting the output.

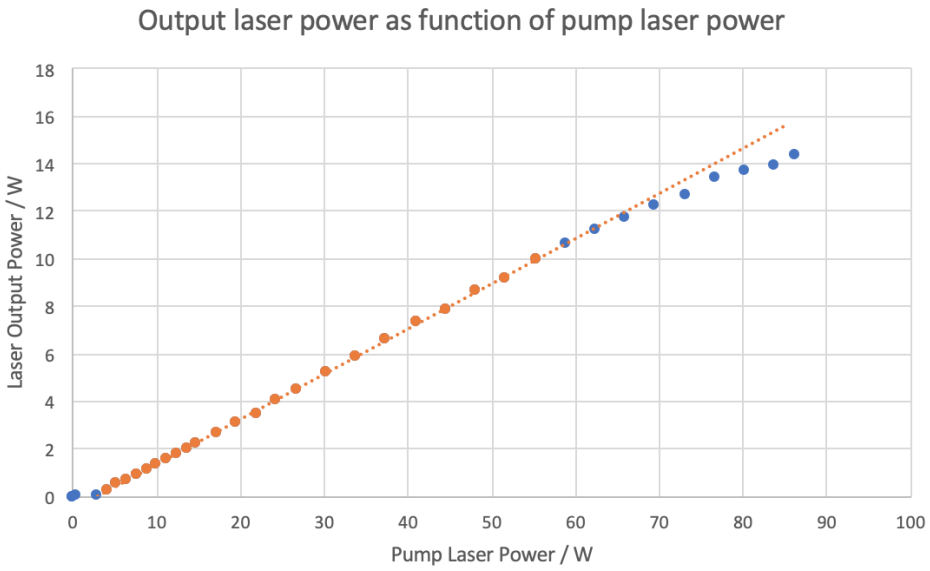



FIGURE 5.7: Output Laser Power as a function of the pump power.

We fitted the orange portion of the data with a linear regression model $y = mx + b$ and the parameters can be seen in table 5.1. The slope is precisely the laser efficiency, which is $\approx 19\%$. If one wants to find the threshold of the laser, one can discover the solution (zero) for the equation of the trend line and realize that the threshold for this system happens when the pump power is equal to $(2.8 \pm 0.1)\ W$.

| | |
|---|---|
| $m$ | 0.1900 |
| $\Delta m$ | 0.0008 |
| $b$ | $-0.53\ W$ |
| $\Delta b$ | $0.02\ W$ |
| $R^2$ | 0.9996 |

TABLE 5.1: Linear regression parameters for orange portion of the data of figure 5.7

Following, it was coupled an Optical Spectrum Analyzer (OSA) to the output of the laser, conveniently attenuated. The main goal was to characterize the spectrum of the final laser source. The results for this analysis can be seen in figure 5.8. The source has its main peak at $\lambda = 1566\ nm$ with $\Delta\lambda = 1.39\ nm$ and a secondary one around 1563.5 $nm$.

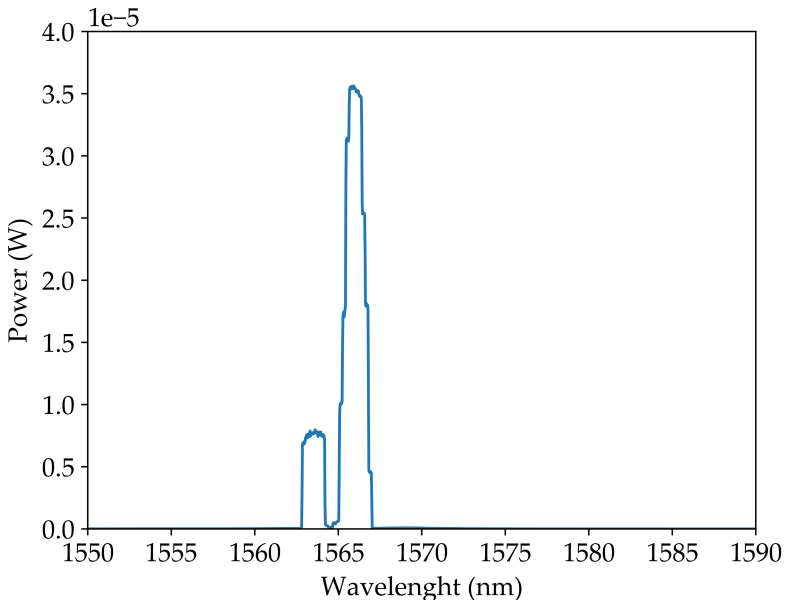



FIGURE 5.8: Spectrum of the Output Laser.

This result is very particular. One can see two peeks of emission. The shift in wavelength for the maximum intensity peak (shifted to 1565 $nm$) is typical from the in-band

pump, and as we increase the length of the fiber, this shift effect will stand out more and more as we increase the fiber length.

## 5.3 Final remarks

We achieved interesting and promising results, regarding this first prototype of the high power fiber laser.

We were able to produce a source around 1566 $nm$, with a slope efficiency of $\approx$ 19%, and maximum output power of 15 $W$. Since we have a pump efficiency of $\approx$ 45.15% converting electrical energy into light energy, our efficiency of the full process is $\approx$ 8.6%.

The next step would be to do a fine alignment to the laser system to measure the $M^2$. This is important because we want to ensure that the laser beam meets all the requirements when it reaches the CubeSat.

It could be also interesting to introduce a second pump laser with a combiner, this way we could analyse the behaviour of the fiber to a higher power (200 $W$), and probably expecting the burning of the fiber at some point, or not. Depending on these results, we could propose another setup for the main laser, such as two-sided pumped fiber, allowing pumping with higher power and more uniform power distribution along the fiber. If the non-linear effects start to be very significant, an architecture like MOPA can be considered, i.e. having several amplification stations with short fibers so that these non-linear effects are minimised.

It is also an objective of the WipTherm project to test this laser with the thermoelectric devices of IFIMUP institute and measure energy efficiencies. The final step would be an energy transfer of 1 $km$, between our laser source and a CubeSat.

# Chapter 6

# Conclusion and Future Work

During this dissertation, we have successfully developed an algorithm capable of simulating atmospheric beam propagation under turbulent conditions and also a 15 $W$ high power fiber laser prototype at 1566 $nm$ in a hybrid configuration.

The algorithm, developed in Python, used to study the propagation of a Gaussian beam through a 7 $km$ turbulent atmosphere predicted a beam deflection of 2.4 $cm$ approximately, using the SLC-Day model for the $C_n^2$ and with 4 different and random phase screens generated with AOtools. Numerical results also showed us that for a typical CubeSat orbit (500 $km$), the minimum waist size that can be achieved corresponds to 0.702 $m$ if one has an initial waist of 0.496 $m$. The value of the final waist 0.702 $m$ is unenthusiastic because the CubeSat effective area is smaller- only 8% of the area would be used.

Throughout this thesis, we were also able to develop a 1566 $nm$ CW high-power erbium double-clad fiber laser source capable of operating at a maximum optical power of 15 $W$, using a hybrid setup. This laser achieved an efficiency of 19%, and has a threshold when the pump optical power is equal to $(2.8 \pm 0.1)W$. The pump laser is a BWT high power high brightness fiber-coupled diode laser from the wavelength-stabilized series at 976 $nm$ with a maximum output power of 140 $W$. Better understanding and improvements on the laser will be done during this year and next year in the framework of the WipTherm project.

In future work, we would be interested in:

- demystifying the changes in the beam profile with the number of phase screens;

- measuring the spatial or temporal fluctuations in the irradiance of the beam profile caused by the phase screens;
- measuring the $M^2$ parameter so we could study how to shape the beam to match the project requirements;
- using a second pump laser with a combiner, and analyse the behaviour on a higher power regime (200 $W$);
- characterizing other types of fiber;
- inspect the use of FBGs instead of mirrors;
- trying a different setup such as two-sided pumped fiber, allowing pumping with higher power and with a more uniform power distribution along the fiber. If the non-linear effects start to be very significant, an architecture like MOPA can be considered, i.e. having several amplification stations with short fibers so that these non-linear effects are minimised.

A prototype for the WipTherm project would be the final step: a laser transferring energy to a CubeSat separated by a distance of 1 $km$.

This work was supported by funding from the European Union's Horizon 2020 research and innovation program under grant agreement No 863307, Ref. H2020-FETOPEN-2018- 2019-2020-01 .

# Appendix A

# Used AOTools functions

During this thesis, it was used widely used the "turbulence.phasescreen.ft_phase_screen" function from the python package AOTools. Below the source code is shown.

```
def ft_phase_screen(r0, N, delta, L0, l0, FFT=None, seed=None):
    """
    Creates a random phase screen with Von Karmen statistics.
    (Schmidt 2010)

    Parameters:
        r0 (float): r0 parameter of scrn in metres
        N (int): Size of phase scrn in pxls
        delta (float): size in Metres of each pxl
        L0 (float): Size of outer-scale in metres
        l0 (float): inner scale in metres

    Returns:
        ndarray: numpy array representing phase screen
    """
    delta = float(delta)
    r0 = float(r0)
    L0 = float(L0)
    l0 = float(l0)

    R = random.SystemRandom(time.time())
    if seed is None:
        seed = int(R.random()*100000)
```

```
    numpy.random.seed(seed)
25
    del_f = 1./(N*delta)
27
    fx = numpy.arange(-N/2., N/2.) * del_f
29
    (fx, fy) = numpy.meshgrid(fx,fx)
31  f = numpy.sqrt(fx**2. + fy**2.)

33  fm = 5.92/l0/(2*numpy.pi)
    f0 = 1./L0
35
    PSD_phi = (0.023*r0**(-5./3.) * numpy.exp(-1*((f/fm)**2)) / (((f**2) + (f0
    **2))**(11./6)))
37
    PSD_phi[int(N/2), int(N/2)] = 0
39
    cn = ((numpy.random.normal(size=(N, N))+1j * numpy.random.normal(size=(N, N))
    ) * numpy.sqrt(PSD_phi)*del_f)
41
    phs = ift2(cn, 1, FFT).real
43
    return phs
```

# Bibliography


[1] Fiber lasers global market report. [Online]. Available: https://www.thebusinessresearchcompany.com/report/fiber-lasers-global-market-report [Cited on page 1.]

[2] Global nanosatellite and microsatellite market report. [Online]. Available: https://www.globenewswire.com/fr/news-release/2021/09/13/2295512/28124/en/Global-Nanosatellite-and-Microsatellite-Market-Report-2021-2026-Rapid-Escalation-of-the-Production-and-Launch-of-Small-Satellites-to-Revolutionize-the-Space-Industry.html [Cited on page 1.]

[3] P. Resende, S. Ferreira Teixeira, and A. Pereira, "Flexible thermoelectric nanogenerators: From numerical simulations to device fabrication," 09 2016. [Cited on page 2.]

[4] Wiptherm website. [Online]. Available: https://wiptherm.eu [Cited on pages xiii and 2.]

[5] J. D. Jackson, *Classical electrodynamics*, 3rd ed. New York, NY: Wiley, 1999. [Online]. Available: http://cdsweb.cern.ch/record/490457 [Cited on pages 5 and 6.]

[6] D. Griffiths, *Introduction to electrodynamics*. Cambridge, United Kingdom New York, NY: Cambridge University Press, 2017. [Cited on page 5.]

[7] Light and health - light spectrum. [Online]. Available: https://juniperuseyewear.se/blue-light-health/ [Cited on pages xiii and 6.]

[8] A. Einstein, "Zur Quantentheorie der Strahlung," *Phys. Z.*, vol. 18, pp. 121–128, 1917. [Cited on pages 7 and 8.]

[9] D. Kleppner, "Rereading einstein on radiation," *Physics Today*, vol. 58, no. 2, pp. 30–33, Feb. 2005. [Online]. Available: https://doi.org/10.1063/1.1897520 [Cited on page 7.]

[10] J. P. Gordon, H. J. Zeiger, and C. H. Townes, "The maser—new type of microwave amplifier, frequency standard, and spectrometer," *Physical Review*, vol. 99, no. 4, pp. 1264–1274, Aug. 1955. [Online]. Available: https://doi.org/10.1103/physrev.99.1264 [Cited on page 10.]

[11] A. L. Schawlow and C. H. Townes, "Infrared and optical masers," *Physical Review*, vol. 112, no. 6, pp. 1940–1949, Dec. 1958. [Online]. Available: https://doi.org/10.1103/physrev.112.1940 [Cited on page 10.]

[12] "The 1964 nobel prize for physics," *Nature*, vol. 204, no. 4962, pp. 923–923, Dec. 1964. [Online]. Available: https://doi.org/10.1038/204923a0 [Cited on pages 10 and 11.]

[13] T. H. MAIMAN, "Stimulated optical radiation in ruby," *Nature*, vol. 187, no. 4736, pp. 493–494, Aug. 1960. [Online]. Available: https://doi.org/10.1038/187493a0 [Cited on pages 10 and 15.]

[14] First laser scheme. [Online]. Available: https://www.llnl.gov/ [Cited on pages xiii and 10.]

[15] C. K. N. Patel, "Continuous-wave laser action on vibrational-rotational transitions of CO2," *Physical Review*, vol. 136, no. 5A, pp. A1187–A1193, Nov. 1964. [Online]. Available: https://doi.org/10.1103/physrev.136.a1187 [Cited on page 10.]

[16] E. I. Gordon and E. F. Labuda, "Gas pumping in continuously operated ion lasers," *Bell System Technical Journal*, vol. 43, no. 4, pp. 1827–1829, Jul. 1964. [Online]. Available: https://doi.org/10.1002/j.1538-7305.1964.tb04114.x [Cited on page 10.]

[17] A. Javan, W. R. Bennett, and D. R. Herriott, "Population inversion and continuous optical maser oscillation in a gas discharge containing a he-ne mixture," *Physical Review Letters*, vol. 6, no. 3, pp. 106–110, Feb. 1961. [Online]. Available: https://doi.org/10.1103/physrevlett.6.106 [Cited on page 10.]

[18] A. D. White, E. I. Gordon, and J. D. Rigden, "OUTPUT POWER OF THE 6328-6328 Å GAS MASER, journal = Applied Physics Letters," vol. 2, no. 5, pp. 91–93, Mar. 1963. [Online]. Available: https://doi.org/10.1063/1.1753793 [Cited on page 10.]

[19] P. P. Sorokin and J. R. Lankard, "Stimulated emission observed from an organic dye, chloro-aluminum phthalocyanine," *IBM Journal of Research and Development*, vol. 10, no. 2, pp. 162–163, Mar. 1966. [Online]. Available: https://doi.org/10.1147/rd.102.0162 [Cited on page 10.]

[20] D. A. G. Deacon, L. R. Elias, J. M. J. Madey, G. J. Ramian, H. A. Schwettman, and T. I. Smith, "First operation of a free-electron laser," *Physical Review Letters*, vol. 38, no. 16, pp. 892–894, Apr. 1977. [Online]. Available: https://doi.org/10.1103/physrevlett.38.892 [Cited on page 10.]

[21] J. J. Kim and N. Sung, "Stimulated emission in optically pumped atomic-copper vapor," *Optics Letters*, vol. 12, no. 11, p. 885, Nov. 1987. [Online]. Available: https://doi.org/10.1364/ol.12.000885 [Cited on page 10.]

[22] J. Moloney, J. Hader, and S. Koch, "Quantum design of semiconductor active materials: laser and amplifier applications," *Laser & Photonics Review*, vol. 1, no. 1, pp. 24–43, Feb. 2007. [Online]. Available: https://doi.org/10.1002/lpor.200610003 [Cited on page 11.]

[23] F. Houtermans, "Über massen-wirkung im optischen spektralgebiet un die möglichkeit absolut negativer absorption für einige fälle von molekülspektren (licht-lawine)," *Helv. Phys. Acta*, vol. 33, p. 933, 1960. [Cited on page 11.]

[24] I. S. Lakoba and S. I. Yakovlenko, "Active media of exciplex lasers (review)," *Soviet Journal of Quantum Electronics*, vol. 10, no. 4, pp. 389–410, Apr. 1980. [Online]. Available: https://doi.org/10.1070/qe1980v010n04abeh010101 [Cited on page 11.]

[25] The nobel prize in physics 1971. nobelprize.org. nobel prize outreach ab 2021. mon. 19 jul 2021. [Online]. Available: https://www.nobelprize.org/prizes/physics/1971/summary/ [Cited on page 11.]

[26] The nobel prize in physics 1981. nobelprize.org. nobel prize outreach ab 2021. sun. 18 jul 2021. [Online]. Available: https://www.nobelprize.org/prizes/physics/1981/summary/ [Cited on page 11.]

[27] The nobel prize in physics 1989. nobelprize.org. nobel prize outreach ab 2021. mon. 19 jul 2021. [Online]. Available: https://www.nobelprize.org/prizes/physics/1989/summary/ [Cited on page 11.]

[28] The nobel prize in physics 1997. nobelprize.org. nobel prize outreach ab 2021. mon. 19 jul 2021. [Online]. Available: https://www.nobelprize.org/prizes/physics/1997/summary [Cited on page 11.]

[29] The nobel prize in physics 2000. nobelprize.org. nobel prize outreach ab 2021. sun. 18 jul 2021. [Online]. Available: https://www.nobelprize.org/prizes/physics/2000/summary/ [Cited on page 11.]

[30] he nobel prize in physics 2001. nobelprize.org. nobel prize outreach ab 2021. mon. 19 jul 2021. [Online]. Available: https://www.nobelprize.org/prizes/physics/2001/summary/ [Cited on page 11.]

[31] The nobel prize in physics 2005. nobelprize.org. nobel prize outreach ab 2021. sun. 18 jul 2021. [Online]. Available: https://www.nobelprize.org/prizes/physics/2005/summary/ [Cited on page 11.]

[32] The nobel prize in physics 2006. nobelprize.org. nobel prize outreach ab 2021. mon. 19 jul 2021. [Online]. Available: https://www.nobelprize.org/prizes/physics/2006/summary/ [Cited on page 11.]

[33] The nobel prize in physics 2018. nobelprize.org. nobel prize outreach ab 2021. sun. 18 jul 2021. [Online]. Available: https://www.nobelprize.org/prizes/physics/2018/summary/ [Cited on page 11.]

[34] M. Draelos, P. Ortiz, R. Qian, C. Viehland, R. McNabb, K. Hauser, A. N. Kuo, and J. A. Izatt, "Contactless optical coherence tomography of the eyes of freestanding individuals with a robotic scanner," *Nature Biomedical Engineering*, vol. 5, no. 7, pp. 726–736, Jul. 2021. [Online]. Available: https://doi.org/10.1038/s41551-021-00753-6 [Cited on page 11.]

[35] Q. T. K. Lai, G. G. K. Yip, J. Wu, J. S. J. Wong, M. C. K. Lo, K. C. M. Lee, T. T. H. D. Le, H. K. H. So, N. Ji, and K. K. Tsia, "High-speed laser-scanning biological microscopy using FACED," *Nature Protocols*, vol. 16, no. 9, pp. 4227–4264, Aug. 2021. [Online]. Available: https://doi.org/10.1038/s41596-021-00576-4 [Cited on page 11.]

[36] J. R. Alonso, R. Barlow, J. M. Conrad, and L. H. Waites, "Medical isotope production with the IsoDAR cyclotron," *Nature Reviews Physics*, vol. 1, no. 9, pp. 533–535, Aug.

2019. [Online]. Available: https://doi.org/10.1038/s42254-019-0095-6 [Cited on page 11.]

[37] T. Muangpool and S. Pullteap, "Reviews on laser cutting technology for industrial applications," in *Third International Conference on Photonics Solutions (ICPS2017)*, T. Mayteevarunyoo, Ed. SPIE, Mar. 2018. [Online]. Available: https://doi.org/10.1117/12.2300955 [Cited on page 11.]

[38] P. A. Norreys, "Laser-driven particle acceleration," *Nature Photonics*, vol. 3, no. 8, pp. 423–425, Aug. 2009. [Online]. Available: https://doi.org/10.1038/nphoton.2009.119 [Cited on page 11.]

[39] L. Hudson and J. Seely, "Laser-produced x-ray sources," *Radiation Physics and Chemistry*, vol. 79, no. 2, pp. 132–138, Feb. 2010. [Online]. Available: https://doi.org/10.1016/j.radphyschem.2009.01.012 [Cited on page 11.]

[40] R. Betti and O. A. Hurricane, "Inertial-confinement fusion with lasers," *Nature Physics*, vol. 12, no. 5, pp. 435–448, May 2016. [Online]. Available: https://doi.org/10.1038/nphys3736 [Cited on page 11.]

[41] H. Füser, R. Judaschke, and M. Bieler, "High-precision frequency measurements in the THz spectral region using an unstabilized femtosecond laser," *Applied Physics Letters*, vol. 99, no. 12, p. 121111, Sep. 2011. [Online]. Available: https://doi.org/10.1063/1.3640234 [Cited on page 12.]

[42] V. Ter-Mikirtychev, *Fundamentals of Fiber Lasers and Fiber Amplifiers*. Springer International Publishing, 2014. [Online]. Available: https://doi.org/10.1007/978-3-319-02338-0 [Cited on page 12.]

[43] "NORIA – the Fiber Bragg Grating manufacturing solution." [Online]. Available: https://hittech.com/nl/portfolio-posts/noria-the-fiber-bragg-grating-manufacturing-solution/ [Cited on pages xiii and 12.]

[44] D. R. Paschotta, "Fiber Lasers." [Online]. Available: https://www.rp-photonics.com/fiber_lasers.html [Cited on pages xiii and 13.]

[45] L. Dong, *Fiber lasers : basics, technology, and applications*. Boca Raton, FL: CRC Press, 2017. [Cited on pages 13 and 50.]

[46] R. Paschotta, *Encyclopedia of laser physics and technology*. Weinheim Chichester: Wiley-VCH John Wiley, distributor, 2008. [Cited on pages xiii and 13.]

[47] C. J. Koester and E. Snitzer, "Amplification in a fiber laser," *Applied Optics*, vol. 3, no. 10, p. 1182, Oct. 1964. [Online]. Available: https://doi.org/10.1364/ao.3.001182 [Cited on page 15.]

[48] R. Mears, L. Reekie, I. Jauncey, and D. Payne, "Low-noise erbium-doped fibre amplifier operating at 1.54m," *Electronics Letters*, vol. 23, no. 19, p. 1026, 1987. [Online]. Available: https://doi.org/10.1049/el:19870719 [Cited on page 15.]

[49] D. Hanna, R. Percival, I. Perry, R. Smart, P. Suni, J. Townsend, and A. Tropper, "Continuous-wave oscillation of a monomode ytterbium-doped fibre laser," *Electronics Letters*, vol. 24, no. 17, p. 1111, 1988. [Online]. Available: https://doi.org/10.1049/el:19880755 [Cited on page 15.]

[50] S. D. Jackson and T. A. King, "High-power diode-cladding-pumped tm-doped silica fiber laser," *Optics Letters*, vol. 23, no. 18, p. 1462, Sep. 1998. [Online]. Available: https://doi.org/10.1364/ol.23.001462 [Cited on page 15.]

[51] S. D. Jackson, "Continuous wave 2.9 m dysprosium-doped fluoride fiber laser," *Applied Physics Letters*, vol. 83, no. 7, pp. 1316–1318, Aug. 2003. [Online]. Available: https://doi.org/10.1063/1.1603353 [Cited on page 15.]

[52] A. C. Tropper, J. N. Carter, R. D. T. Lauder, D. C. Hanna, S. T. Davey, and D. Szebesta, "Analysis of blue and red laser performance of the infrared-pumped praseodymium-doped fluoride fiber laser," *Journal of the Optical Society of America B*, vol. 11, no. 5, p. 886, May 1994. [Online]. Available: https://doi.org/10.1364/josab.11.000886 [Cited on page 15.]

[53] N. Simakov, A. Hemming, W. A. Clarkson, J. Haub, and A. Carter, "A cladding-pumped, tunable holmium doped fiber laser," *Optics Express*, vol. 21, no. 23, p. 28415, Nov. 2013. [Online]. Available: https://doi.org/10.1364/oe.21.028415 [Cited on page 15.]

[54] E. Desurvire, *Erbium-Doped Fiber Amplifiers: Principles and Applications*. John Wiley Sons, 1994. [Cited on page 15.]

[55] R. Maurer, "Optical waveguide light source," *United States patent 3808549*, 1974. [Cited on page 15.]

[56] E. Snitzer, H. Po, F. Hakimi, R. Tumminelli, and B. McCollum, "DOUBLE CLAD, OFFSET CORE nd FIBER LASER," 1988. [Online]. Available: https://doi.org/10.1364/ofs.1988.pd5 [Cited on page 15.]

[57] N. Boetti, D. Pugliese, E. Ceci-Ginistrelli, J. Lousteau, D. Janner, and D. Milanese, "Highly doped phosphate glass fibers for compact lasers and amplifiers: A review," *Applied Sciences*, vol. 7, no. 12, p. 1295, Dec. 2017. [Online]. Available: https://doi.org/10.3390/app7121295 [Cited on pages xiii and 16.]

[58] D. J. Richardson, J. Nilsson, and W. A. Clarkson, "High power fiber lasers: current status and future perspectives [invited]," *Journal of the Optical Society of America B*, vol. 27, no. 11, p. B63, Oct. 2010. [Online]. Available: https://doi.org/10.1364/josab.27.000b63 [Cited on page 16.]

[59] D. Marcuse, "Influence of curvature on the losses of doubly clad fibers," *Applied Optics*, vol. 21, no. 23, p. 4208, Dec. 1982. [Online]. Available: https://doi.org/10.1364/ao.21.004208 [Cited on page 16.]

[60] M. E. Fermann, "Single-mode excitation of multimode fibers with ultrashort pulses," *Optics Letters*, vol. 23, no. 1, p. 52, Jan. 1998. [Online]. Available: https://doi.org/10.1364/ol.23.000052 [Cited on page 16.]

[61] T. Bhutta, J. I. Mackenzie, D. P. Shepherd, and R. J. Beach, "Spatial dopant profiles for transverse-mode selection in multimode waveguides," *Journal of the Optical Society of America B*, vol. 19, no. 7, p. 1539, Jul. 2002. [Online]. Available: https://doi.org/10.1364/josab.19.001539 [Cited on page 16.]

[62] A. E. Siegman, "Gain-guided, index-antiguided fiber lasers," *Journal of the Optical Society of America B*, vol. 24, no. 8, p. 1677, Jul. 2007. [Online]. Available: https://doi.org/10.1364/josab.24.001677 [Cited on page 16.]

[63] Donlagic, "In-line higher order mode filters based on long highly uniform fiber tapers," *Journal of Lightwave Technology*, vol. 24, no. 9, pp. 3532–3539, Sep. 2006. [Online]. Available: https://doi.org/10.1109/jlt.2006.878497 [Cited on page 16.]

[64] J. Knight, T. Birks, R. Cregan, P. Russell, and J.-P. de Sandro, "Large mode area photonic crystal fibre," *Electronics Letters*, vol. 34, no. 13, p. 1347, 1998. [Online]. Available: https://doi.org/10.1049/el:19980965 [Cited on page 16.]

[65] T. Eidam, J. Rothhardt, F. Stutzki, F. Jansen, S. Hädrich, H. Carstens, C. Jauregui, J. Limpert, and A. Tünnermann, "Fiber chirped-pulse amplification system emitting 38 GW peak power," *Optics Express*, vol. 19, no. 1, p. 255, Dec. 2010. [Online]. Available: https://doi.org/10.1364/oe.19.000255 [Cited on page 17.]

[66] P. Zhou, X. Wang, H. Xiao, Y. Ma, and J. Chen, "Review on recent progress on yb-doped fiber laser in a variety of oscillation spectral ranges," *Laser Physics*, vol. 22, no. 5, pp. 823–831, Apr. 2012. [Online]. Available: https://doi.org/10.1134/s1054660x12050404 [Cited on page 17.]

[67] H. Pask, R. Carman, D. Hanna, A. Tropper, C. Mackechnie, P. Barber, and J. Dawes, "Ytterbium-doped silica fiber lasers: versatile sources for the 1-1.2 m region," *IEEE Journal of Selected Topics in Quantum Electronics*, vol. 1, no. 1, pp. 2–13, Apr. 1995. [Online]. Available: https://doi.org/10.1109/2944.468377 [Cited on page 17.]

[68] P. Barua, E. Sekiya, K. Saito, and A. Ikushima, "Influences of yb3 ion concentration on the spectroscopic properties of silica glass," *Journal of Non-Crystalline Solids*, vol. 354, no. 42-44, pp. 4760–4764, Nov. 2008. [Online]. Available: https://doi.org/10.1016/j.jnoncrysol.2008.04.020 [Cited on page 17.]

[69] F. Beier, C. Hupel, S. Kuhn, S. Hein, J. Nold, F. Proske, B. Sattler, A. Liem, C. Jauregui, J. Limpert, N. Haarlammert, T. Schreiber, R. Eberhardt, and A. Tünnermann, "Single mode 43 kW output power from a diode-pumped yb-doped fiber amplifier," *Optics Express*, vol. 25, no. 13, p. 14892, Jun. 2017. [Online]. Available: https://doi.org/10.1364/oe.25.014892 [Cited on page 17.]

[70] E. A. Shcherbakov, V. V. Fomin, A. A. Abramov, A. A. Ferin, D. V. Mochalov, and V. P. Gapontsev, "Industrial grade 100 kW power CW fiber laser," 2013. [Online]. Available: https://doi.org/10.1364/assl.2013.ath4a.2 [Cited on page 17.]

[71] J. A. Shaw and P. W. Nugent, "Physics principles in radiometric infrared imaging of clouds in the atmosphere," *European Journal of Physics*, vol. 34, no. 6, pp. S111–S121, Oct. 2013. [Online]. Available: https://doi.org/10.1088/0143-0807/34/6/s111 [Cited on page 18.]

[72] S. Jackson, "The spectroscopic and energy transfer characteristics of the rare earth ions used for silicate glass fibre lasers operating in the shortwave infrared," *Laser & Photonics Review*, vol. 3, no. 5, pp. 466–482, Sep. 2009. [Online]. Available: https://doi.org/10.1002/lpor.200810058 [Cited on page 18.]

[73] S. D. Jackson, "Cross relaxation and energy transfer upconversion processes relevant to the functioning of 2 m tm3-doped silica fibre lasers," *Optics Communications*, vol. 230, no. 1-3, pp. 197–203, Jan. 2004. [Online]. Available: https://doi.org/10.1016/j.optcom.2003.11.045 [Cited on page 18.]

[74] N. Boetti, D. Pugliese, E. Ceci-Ginistrelli, J. Lousteau, D. Janner, and D. Milanese, "Highly doped phosphate glass fibers for compact lasers and amplifiers: A review," *Applied Sciences*, vol. 7, no. 12, p. 1295, Dec. 2017. [Online]. Available: https://doi.org/10.3390/app7121295 [Cited on pages xiii and 18.]

[75] P. Myslinski, D. Nguyen, and J. Chrostowski, "Effects of concentration on the performance of erbium-doped fiber amplifiers," *Journal of Lightwave Technology*, vol. 15, no. 1, pp. 112–120, 1997. [Online]. Available: https://doi.org/10.1109/50.552118 [Cited on page 19.]

[76] L. V. Kotov, M. E. Likhachev, M. M. Bubnov, O. I. Medvedkov, M. V. Yashkov, A. N. Guryanov, J. Lhermite, S. Février, and E. Cormier, "75 w 40% efficiency single-mode all-fiber erbium-doped laser cladding pumped at 976 nm," *Optics Letters*, vol. 38, no. 13, p. 2230, Jun. 2013. [Online]. Available: https://doi.org/10.1364/ol.38.002230 [Cited on page 19.]

[77] M. Fermann, D. Hanna, D. Shepherd, P. Suni, and J. Townsend, "Efficient operation of an yb-sensitised er fibre laser at 1.56 m," *Electronics Letters*, vol. 24, no. 18, p. 1135, 1988. [Online]. Available: https://doi.org/10.1049/el:19880772 [Cited on page 19.]

[78] D. Y. Shen, J. K. Sahu, and W. A. Clarkson, "Highly efficient er, yb-doped fiber laser with 188w free-running and 100w tunable output power," *Optics Express*, vol. 13, no. 13, p. 4916, 2005. [Online]. Available: https://doi.org/10.1364/opex.13.004916 [Cited on page 19.]

[79] Y. Jeong, A. Harker, M. Lovelady, A. Piper, S. Yoo, C. A. Codemard, J. Nilsson, J. K. Sahu, D. N. Payne, R. Horley, P. Turner, and L. Hickey, "Erbium:ytterbium codoped

large-core fiber laser with 297-w continuous-wave output power," *IEEE Journal of Selected Topics in Quantum Electronics*, vol. 13, no. 3, pp. 573–579, May 2007. [Online]. Available: https://doi.org/10.1109/jstqe.2007.897178 [Cited on page 19.]

[80] X. Zhao, Q. Han, D. Wang, H. Hu, K. Ren, J. Jiang, and T. Liu, "Optimal design of high-power cascade co-pumping er/yb-codoped fiber lasers," *Optics Letters*, vol. 44, no. 5, p. 1100, Feb. 2019. [Online]. Available: https://doi.org/10.1364/ol.44.001100 [Cited on page 19.]

[81] V. Kuhn, P. Weßels, J. Neumann, and D. Kracht, "Stabilization and power scaling of cladding pumped er:yb-codoped fiber amplifier via auxiliary signal at 1064 nm," *Optics Express*, vol. 17, no. 20, p. 18304, Sep. 2009. [Online]. Available: https://doi.org/10.1364/oe.17.018304 [Cited on page 19.]

[82] K. Schuster, S. Unger, C. Aichele, F. Lindner, S. Grimm, D. Litzkendorf, J. Kobelke, J. Bierlich, K. Wondraczek, and H. Bartelt, "Material and technology trends in fiber optics," *Advanced Optical Technologies*, vol. 3, no. 4, Jan. 2014. [Online]. Available: https://doi.org/10.1515/aot-2014-0010 [Cited on page 19.]

[83] R. Dauliat, A. Benoît, D. Darwich, R. Jamier, J. Kobelke, S. Grimm, K. Schuster, and P. Roy, "Demonstration of a homogeneous yb-doped core fully aperiodic large-pitch fiber laser," *Applied Optics*, vol. 55, no. 23, p. 6229, Aug. 2016. [Online]. Available: https://doi.org/10.1364/ao.55.006229 [Cited on page 19.]

[84] M.-A. Malleville, R. Dauliat, A. Benoît, B. Leconte, D. Darwich, R. du Jeu, R. Jamier, K. Schuster, and P. Roy, "Experimental study of the mode instability onset threshold in high-power FA-LPF lasers," *Optics Letters*, vol. 42, no. 24, p. 5230, Dec. 2017. [Online]. Available: https://doi.org/10.1364/ol.42.005230 [Cited on page 19.]

[85] O.Svelto, *Lasers*. Sringer US, 2010. [Cited on pages 21 and 22.]

[86] A. Siegman, *Lasers*. Oxford University Press, Oxford, U. K., 1986. [Cited on page 21.]

[87] K. Khare, *Fourier Optics and Computational Imaging*. John Wiley & Sons, Ltd, Sep. 2015. [Online]. Available: https://doi.org/10.1002/9781118900352 [Cited on page 26.]

[88] V. Van Gogh, "The starry night," *Museum of Modern Art, New York*, 1889. [Cited on pages xiii and 27.]

[89] L. Sjöqvist, M. Henriksson, and O. Steinvall, "Simulation of laser beam propagation over land and sea using phase screens: a comparison with experimental data," in *Technologies for Optical Countermeasures II Femtosecond Phenomena II and Passive Millimetre-Wave and Terahertz Imaging II*, D. H. Titterton, S. M. Kirkpatrick, R. Stoian, R. Appleby, J. M. Chamberlain, and K. A. Krapels, Eds. SPIE, Oct. 2005. [Online]. Available: https://doi.org/10.1117/12.630655 [Cited on page 28.]

[90] A. Boime, *Van Gogh Starry night*. New York: Voyager, 1995. [Cited on page 28.]

[91] V. S. R. Gudimetla, R. B. Holmes, T. C. Farrell, and J. Lucas, "Phase screen simulations of laser propagation through non-kolmogorov atmospheric turbulence," in *Atmospheric Propagation VIII*, L. M. W. Thomas and E. J. Spillar, Eds. SPIE, May 2011. [Online]. Available: https://doi.org/10.1117/12.887595 [Cited on page 28.]

[92] E. M. Whitfield, P. P. Banerjee, and J. W. Haus, "Propagation of gaussian beams through a modified von karman phase screen," in *Laser Communication and Propagation through the Atmosphere and Oceans*, A. M. J. van Eijk, C. C. Davis, S. M. Hammel, and A. K. Majumdar, Eds. SPIE, Oct. 2012. [Online]. Available: https://doi.org/10.1117/12.932277

[93] L. C. Andrews, R. L. Phillips, and A. R. Weeks, "Propagation of a gaussian-beam wave through a random phase screen," *Waves in Random Media*, vol. 7, no. 2, pp. 229–244, Apr. 1997. [Online]. Available: https://doi.org/10.1088/0959-7174/7/2/005

[94] X. Zhu and J. Kahn, "Free-space optical communication through atmospheric turbulence channels," *IEEE Transactions on Communications*, vol. 50, no. 8, pp. 1293–1300, Aug. 2002. [Online]. Available: https://doi.org/10.1109/tcomm.2002.800829 [Cited on page 28.]

[95] V. A. Krasil'nikov and V. I. Tatarsky, "Atmospheric turbulence and radio-wave propagation," 1962. [Cited on page 28.]

[96] U. Frisch, *Turbulence: The Legacy of AN Kolmogorov*. Cambridge University Press, 1995. [Cited on page 28.]

[97] T. de Karman and L. Howarth, "On the statistical theory of isotropic turbulence," *Proceedings of the Royal Society of London. Series A - Mathematical and Physical Sciences*, vol. 164, no. 917, pp. 192–215, Jan. 1938. [Online]. Available: https://doi.org/10.1098/rspa.1938.0013 [Cited on page 28.]

[98] L. Andrews, *Laser beam propagation through random media*. Bellingham, Wash: SPIE, 2005. [Cited on page 28.]

[99] J. D. Schmidt, *Numerical Simulation of Optical Wave Propagation with Examples in MATLAB*. SPIE, Jul. 2010. [Online]. Available: https://doi.org/10.1117/3.866274 [Cited on pages xiii and 28.]

[100] J. Goodman, *Statistical optics*. New York: Wiley, 2000. [Cited on page 29.]

[101] F. Roddier, "V the effects of atmospheric turbulence in optical astronomy," in *Progress in Optics*. Elsevier, 1981, pp. 281–376. [Online]. Available: https://doi.org/10.1016/s0079-6638(08)70204-x [Cited on page 29.]

[102] M. R. Chatterjee and F. H. A. Mohamed, "Investigation of profiled beam propagation through a turbulent layer and temporal statistics of diffracted output for a modified von karman phase screen," in *Free-Space Laser Communication and Atmospheric Propagation XXVI*, H. Hemmati and D. M. Boroson, Eds. SPIE, Mar. 2014. [Online]. Available: https://doi.org/10.1117/12.2033442 [Cited on page 29.]

[103] L. R. Tsvang, "Microstructure of temperature fields in the free atmosphere," *Radio Science*, vol. 4, no. 12, pp. 1175–1177, Dec. 1969. [Online]. Available: https://doi.org/10.1029/rs004i012p01175 [Cited on page 29.]

[104] D. Fried, "Remote probing of the optical strength of atmospheric turbulence and of wind velocity," *Proceedings of the IEEE*, vol. 57, no. 4, pp. 415–420, 1969. [Online]. Available: https://doi.org/10.1109/proc.1969.6995

[105] J. W. Strohbehn, "Remote sensing of clear-air turbulence," *Journal of the Optical Society of America*, vol. 60, no. 7, p. 948, Jul. 1970. [Online]. Available: https://doi.org/10.1364/josa.60.000948

[106] R. S. Lawrence, G. R. Ochs, and S. F. Clifford, "Measurements of atmospheric turbulence relevant to optical propagation," *Journal of the Optical Society of America*,

vol. 60, no. 6, p. 826, Jun. 1970. [Online]. Available: https://doi.org/10.1364/josa.60.000826

[107] J. L. Bufton, P. O. Minott, M. W. Fitzmaurice, and P. J. Titterton, "Measurements of turbulence profiles in the troposphere," *Journal of the Optical Society of America*, vol. 62, no. 9, p. 1068, Sep. 1972. [Online]. Available: https://doi.org/10.1364/josa.62.001068

[108] D. W. Beran, W. H. Hooke, and S. F. Clifford, "Acoustic echo-sounding techniques and their application to gravity-wave, turbulence, and stability studies," *Boundary-Layer Meteorology*, vol. 4, no. 1-4, pp. 133–153, Apr. 1973. [Online]. Available: https://doi.org/10.1007/bf02265228

[109] G. R. Ochs, T. i Wang, R. S. Lawrence, and S. F. Clifford, "Refractive-turbulence profiles measured by one-dimensional spatial filtering of scintillations," *Applied Optics*, vol. 15, no. 10, p. 2504, Oct. 1976. [Online]. Available: https://doi.org/10.1364/ao.15.002504

[110] T. E. VanZandt, J. L. Green, K. S. Gage, and W. L. Clark, "Vertical profiles of refractivity turbulence structure constant: Comparison of observations by the sunset radar with a new theoretical model," *Radio Science*, vol. 13, no. 5, pp. 819–829, Sep. 1978. [Online]. Available: https://doi.org/10.1029/rs013i005p00819

[111] R. B. Chadwick and K. P. Moran, "Long-term measurements ofCn2in the boundary layer," *Radio Science*, vol. 15, no. 2, pp. 355–361, Mar. 1980. [Online]. Available: https://doi.org/10.1029/rs015i002p00355

[112] F. D. Eaton, W. A. Peterson, J. R. Hines, K. R. Peterman, R. E. Good, R. R. Beland, and J. H. Brown, "Comparisons of VHF radar, optical, and temperature fluctuation measurements ofC n 2 , r 0 and? 0," *Theoretical and Applied Climatology*, vol. 39, no. 1, pp. 17–29, 1988. [Online]. Available: https://doi.org/10.1007/bf00867654

[113] F. Dalaudier, M. Crochet, and C. Sidi, "Direct comparison between in situ and radar measurements of temperature fluctuation spectra: A puzzling result," *Radio Science*, vol. 24, no. 3, pp. 311–324, May 1989. [Online]. Available: https://doi.org/10.1029/rs024i003p00311

[114] R. E. Good, R. R. Beland, E. A. Murphy, J. H. Brown, and E. M. Dewan, "Atmospheric models of optical turbulence," in *Modeling of the Atmosphere*. SPIE, Aug. 1988. [Online]. Available: https://doi.org/10.1117/12.975626

[115] W. W. Brown, M. C. Roggemann, T. J. Schulz, T. C. Havens, J. T. Beyer, and L. J. Otten, "Measurement and data-processing approach for estimating the spatial statistics of turbulence-induced index of refraction fluctuations in the upper atmosphere," *Applied Optics*, vol. 40, no. 12, p. 1863, Apr. 2001. [Online]. Available: https://doi.org/10.1364/ao.40.001863

[116] J. T. Beyer, M. C. Roggemann, L. J. Otten, T. J. Schulz, T. C. Havens, and W. W. Brown, "Experimental estimation of the spatial statistics of turbulence-induced index of refraction fluctuations in the upper atmosphere," *Applied Optics*, vol. 42, no. 6, p. 908, Feb. 2003. [Online]. Available: https://doi.org/10.1364/ao.42.000908 [Cited on page 29.]

[117] R. R. Parenti and R. J. Sasiela, "Laser-guide-star systems for astronomical applications," *Journal of the Optical Society of America A*, vol. 11, no. 1, p. 288, Jan. 1994. [Online]. Available: https://doi.org/10.1364/josaa.11.000288 [Cited on pages 29 and 37.]

[118] J. P. McHugh, G. Y. Jumper, and M. Chun, "Balloon thermosonde measurements over mauna kea and comparison with seeing measurements," *Publications of the Astronomical Society of the Pacific*, vol. 120, no. 874, pp. 1318–1324, Dec. 2008. [Online]. Available: https://doi.org/10.1086/595871 [Cited on page 30.]

[119] M. J. Townson, O. J. D. Farley, G. O. de Xivry, J. Osborn, and A. P. Reeves, "AOtools: a python package for adaptive optics modelling and analysis," *Optics Express*, vol. 27, no. 22, p. 31316, Oct. 2019. [Online]. Available: https://doi.org/10.1364/oe.27.031316 [Cited on page 30.]

[120] F. Assémat, R. Wilson, and E. Gendron, "Method for simulating infinitely long and non stationary phase screens with optimized memory storage," *Optics Express*, vol. 14, no. 3, p. 988, 2006. [Online]. Available: https://doi.org/10.1364/oe.14.000988 [Cited on pages 30 and 31.]

[121] D. L. Fried and T. Clark, "Extruding kolmogorov-type phase screen ribbons," *Journal of the Optical Society of America A*, vol. 25, no. 2, p. 463, Jan. 2008. [Online]. Available: https://doi.org/10.1364/josaa.25.000463 [Cited on page 31.]

[122] Bwt high power high brightness fiber-coupled diode laser wavelength-stabilized series 976 nm - 140w. [Online]. Available: https://www.bwt-bj.com/product/202001/06/976nm%20140W%20%20Wavelengh-Stabilized%20High%20Power%20Diode%20Laser-N1.pdf [Cited on page 52.]

[123] P. Zhou, X. Wang, H. Xiao, Y. Ma, and J. Chen, "Review on recent progress on yb-doped fiber laser in a variety of oscillation spectral ranges," *Laser Physics*, vol. 22, no. 5, pp. 823–831, Apr. 2012. [Online]. Available: https://doi.org/10.1134/s1054660x12050404 [Cited on page 52.]